Dynamics of sting-jet storm "Egon" over continental Europe: impact of surface properties and model resolution

Lea Eisenstein, Florian Pantillon, Peter Knippertz

Received: 5 April 2019 | Revised: 11 September 2019 | Accepted: 13 September 2019 | Published on: 2 December 2019

DOI: 10.1002/qj.3666

RESEARCH ARTICLE

Quarterly Journal of the Royal Meteorological Society RMetS

Dynamics of sting-jet storm *Egon* over continental Europe: Impact of surface properties and model resolution

Lea Eisenstein[1] | Florian Pantillon[1,2] | Peter Knippertz[1]

[1]Institute of Meteorology and Climate Research, Karlsruhe Institute of Technology, Karlsruhe, Germany

[2]Laboratoire d'Aérologie, Université de Toulouse, CNRS, UPS, Toulouse, France

Correspondence
Lea Eisenstein, Institute of Meteorology and Climate Research, Karlsruhe Institute of Technology, Wolfgang-Gaede-Strasse 1, 76131 Karlsruhe, Germany.
Email: lea.eisenstein@kit.edu

Funding information
German Research Foundation (DFG). Grant Number: SFB / TRR 165 "Waves to Weather".

Abstract

Intense Shapiro–Keyser cyclones are often accompanied by a sting jet (SJ), an air stream that descends from the cloud head into the frontal-fracture region and can cause extreme surface gusts. Previous case-studies have concentrated on the North Atlantic and the British Isles. Here we present the first-ever detailed analysis of an SJ over continental Europe and investigate the influence of topography on its dynamical evolution based on observations and high-resolution simulations using the ICOsahedral Nonhydrostatic model (ICON). Windstorm *Egon* intensified over the English Channel and then tracked from northern France to Poland on 12–13 January 2017, causing gusts of almost 150 $km \cdot h^{-1}$ and important damage. ICON reproduces the storm dynamics, although it delays the explosive deepening, shifts the track southward over Belgium and Germany and underestimates gusts over land. Storm characteristics show weak sensitivity to varying grid spacing between 1.6 and 6.5 km, while switching off the convection parametrization at 3.3 km grid spacing improves correlations with surface observations but deteriorates the mean error. Trajectories reveal typical SJ characteristics such as mid-level descent, strong acceleration and conditional symmetric and other mesoscale instabilities, while evaporative cooling is stronger than in previous cases from the literature, preventing drying during descent. The SJ identification and the occurrence of mesoscale instabilities depend considerably on model resolution, convective parametrization, output frequency and employed thresholds for trajectory selection. Sensitivity experiments with modified surface characteristics show that the combined effects of warm-air blocking by the Alps, higher roughness over land and reduced surface fluxes cause *Egon* to fill more quickly and to move on a faster, more northern track across Germany. While the SJ response is complex, showing some compensating effects, surface gusts strongly increase when roughness is reduced. These results suggest that weather forecasters in continental Europe should be more aware of the potential risks associated with SJs.

KEYWORDS

continental Europe, evaporative cooling, high resolution, mesoscale instability, sting jet, topography, windstorm

1 | INTRODUCTION

The most damaging wind hazards over Europe are associated with intense wintertime extratropical cyclones, which in addition can cause heavy precipitation and flooding (Catto, 2016). Such storms have a strong socio-economic impact through fatalities, damaged infrastructure and forests as well as disruption to electricity and transportation systems. Insured damages reach billions of euros in intense cases (e.g. *Lothar* (December 1999: Wernli *et al.*, 2002; Schmoeckel and Kottmeier, 2008), *Kyrill* (January 2007: Fink *et al.*, 2009)).

Strong winds in extratropical cyclones are mainly caused by low-level jets associated with conveyor belts accompanying the fronts, namely the warm conveyor belt jet or warm jet (hereafter WJ) and the cold conveyor belt jet or cold jet (hereafter CJ), as well as frontal convection (Hewson and Neu, 2015; Earl *et al.*, 2017). However, Browning (2004) and Clark *et al.* (2005) demonstrated in their research on the Great Storm of October 1987 that a small-scale and short-lived wind phenomenon, which occurs close to the bent-back front of a Shapiro–Keyser cyclone and is not associated with a conveyor belt, can cause extreme winds. Browning (2004) called this phenomenon a sting jet (SJ). Since then, a number of realistic and idealised case-studies have investigated SJ storms and their dynamics. Climatologies suggest that up to one-third of North Atlantic storms may develop an SJ at some stage (Martínez-Alvarado *et al.*, 2012; Hart *et al.*, 2017). Since SJs can cause damaging wind speeds and are challenging to forecast accurately, it is important to fully understand this phenomenon and to predict it sufficiently well, even more so as the potential of SJ storms may increase with climate change (Knippertz *et al.*, 2018; Martínez-Alvarado *et al.*, 2018).

SJs have broadly been defined as air streams descending from within the cloud head into the frontal-fracture region of a Shapiro–Keyser cyclone (Clark and Gray, 2018). In early stages the SJ is located above the CJ and later on reaches the lower troposphere ahead of it, before the CJ wraps further around the cyclone centre. This makes the SJ hard to discern from the CJ. SJs typically accelerate while descending on slanted surfaces of constant wet-bulb potential temperature before entering the planetary boundary layer, where they create strong near-surface winds and gusts (Baker *et al.*, 2014). These characteristics are mostly consistent in previous literature but do not define an SJ and are not required to confirm its presence. After exiting the cloud head, relative humidity usually decreases markedly. Browning (2004) first hypothesised that conditional symmetric instability (CSI) and evaporative cooling are important factors in the evolution of an SJ. However, following studies found both supporting (e.g. Gray *et al.*, 2011; Martínez-Alvarado *et al.*, 2014; Volonté *et al.*, 2018), contradicting (e.g. Smart and Browning, 2014; Slater *et al.*, 2015) and neutral evidence (Coronel *et al.*, 2016) for CSI contribution. Similarly, the contribution of evaporative cooling has been confirmed in some cases (e.g. Clark *et al.*, 2005; Browning *et al.*, 2015) and dismissed in others (e.g. Baker, 2009; Baker *et al.*, 2014; Smart and Browning, 2014; Coronel *et al.*, 2016). Schultz and Sienkiewicz (2013) claim that frontal dynamics are more important than small-scale moist processes and that an SJ is related to frontolysis at the tip of the bent-back front (see also Slater *et al.*, 2015; 2017; Coronel *et al.*, 2016). These results suggest mixed contributions and some case-to-case variability in SJ dynamics. Accordingly, Volonté *et al.* (2018) found that both mesoscale instabilities and frontal dynamics contributed to the strength of the SJ of storm *Tini* (12 February 2014) in high-resolution simulations. Using a lower resolution, just the contribution of frontal dynamics is evident. To resolve mesoscale instabilities and thus CSI, horizontal grid spacing of 10 to 12 km or finer as well as vertical aspect ratio of 1:50 or below are needed (Clark *et al.*, 2005). This criterion is not satisfied in, for example, Slater *et al.* (2015; 2017), who used a grid spacing of 20 km. Most SJ case-studies are dedicated to cyclones over the North Atlantic and the British Isles with some of these storms crossing northern Europe later in their life cycle (e.g. *Christian* in October 2013: Browning *et al.*, 2015; Pantillon *et al.*, 2018). Brâncuş *et al.* (2019) investigate a cyclone, which developed an SJ over the Black Sea in December 2012, showing that SJs can also occur in more continentally influenced areas. To the best of our knowledge, however, no SJ has been documented to occur fully over continental Europe. It is therefore unclear to what extent and in what way SJs are impacted by topography.

This article focuses on windstorm *Egon*, which underwent explosive cyclogenesis over the English Channel and then tracked across northern France, Belgium, Luxembourg and Germany during the night of 12 to 13 January 2017. The storm left a pronounced gust footprint from northern France to south-central Germany and caused insured damages of EUR 275 million (PERILS AG, 2018). Extreme gusts of almost 150 $km \cdot h^{-1}$ to the south of the cyclone centre (Figure 1a) and banded structures in the cloud head around midnight of 13 January 2017 (Figure 1b) suggest the presence of an SJ. The banded structure can also be seen in radar imagery over western Germany (not shown). This potentially makes *Egon* the first reported SJ case over central Europe. For a detailed analysis of the dynamics of this storm, we employ a series of high-resolution numerical experiments using the ICOsahedral Nonhydrostatic (ICON) model (Zängl *et al.*, 2015) in limited-area mode (ICON-LAM) and evaluate them with surface observations of wind gusts. Using grid spacings down to 1.6 km and up to 90 vertical levels allows an adequate representation of orography and small-scale processes such as mesoscale and convective instabilities. In these simulations, the SJ is identified on the basis of descending high-wind trajectories. Sensitivities are tested with respect to

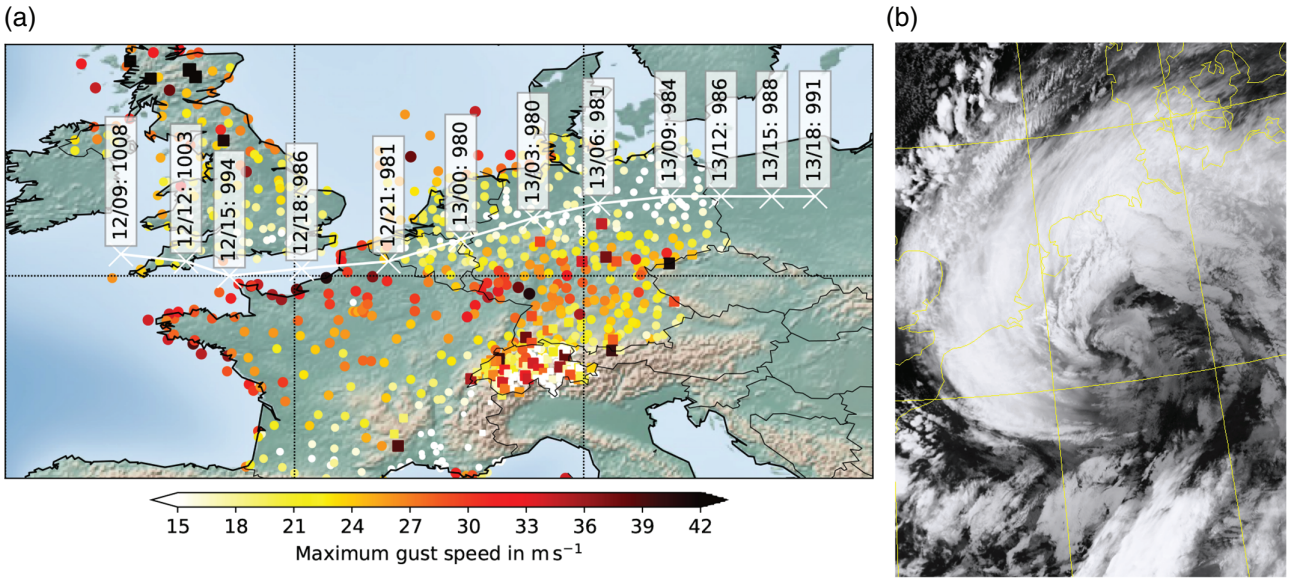

FIGURE 1 Overview of storm *Egon* in observations and ICON analysis: (a) analysed cyclone track and maximum observed 10 m wind gust speeds ($m \cdot s^{-1}$) from 12 January 2017, 0000 UTC to 14 January 2017, 0000 UTC; (b) infrared satellite image (VIIRS, Channel 115) of the cloud head of windstorm *Egon* at 13 January 2017, 0046 UTC. Boxes in (a) display time as day/hour UTC as well as core pressure in hPa, while square markers indicate mountain stations defined by an altitude above 800 m

horizontal and vertical resolution, use of convective parametrization, time step for trajectory computation and thresholds used in SJ identification. Furthermore, the unprecedented occurrence of an SJ over continental Europe was used to test sensitivities to orography, surface roughness and surface fluxes for the first time.

The article is structured as follows. Section 2 describes the employed data, model set-up and diagnostic tools. A synoptic overview of storm *Egon* and an evaluation of model simulations are presented in section 3. An analysis of SJ characteristics using trajectories can be found in section 4, where the sensitivity to model configuration, trajectory computation and SJ selection criteria are also discussed. Section 5 then concentrates on the role of topography using a series of sensitivity experiments. Lastly, the results of this study are summarised and discussed in section 6.

2 | DATA AND METHODS

2.1 | Observations

For the validation of our simulations, two sources of station data were used. Daily maximum gust speeds for 12 and 13 January 2017 were available for 812 SYNOP stations from Belgium, France, Germany, Luxembourg, the Netherlands, Switzerland and the United Kingdom (Figure 1a). For Germany, hourly data of mean wind speed (285 stations), mean-sea-level pressure (192 stations), precipitation (947 stations), relative humidity and temperature at 2 m (501 stations) were available from the surface network of the Deutscher Wetterdienst (DWD).

2.2 | Model experiments

This study is largely based on model experiments performed with the ICON modelling framework (Zängl *et al.*, 2015). ICON is based on an icosahedral-triangular Arakawa C grid, where 20 equilateral triangles of an icosahedron are iteratively split into smaller triangles up to the desired resolution. This has the advantage of a homogeneous grid covering the globe, such that the distance between grid points does not depend on latitude. Furthermore, this kind of grid avoids the problem of singularity at the poles. The model equations are fully compressible and use the velocity components normal and tangential to the triangle edge, while the vertical discretisation is in generalised smooth-level vertical coordinates (SLEVE) described by Leuenberger *et al.* (2010). Since 2015 the DWD has been running operational forecasts with ICON globally (ICON-G) with a refined nest over Europe (ICON-EU), using 13 km horizontal grid spacing in the former and 6.5 km in the latter case.

In this work, ICON is used in limited area mode (LAM), which is planned to become operational at DWD in the near future for high-resolution regional forecasts. The model domain contains the volume between 40°N to 60°N, 20°W to 20°E (Figure 2) and from the surface up to 23 km. Initial conditions are the operational ICON-EU 3 h first-guess valid on 12 January 2017, 0000 UTC, while lateral boundary conditions are given every 3 h by the operational ICON-EU forecast from 12 to 14 January 2017, 0000 UTC. The first guess is used rather than the analysis, because it reduces initial noise and contains additional fields that are mandatory to initialise ICON-LAM simulations. The operational ICON-EU set-up

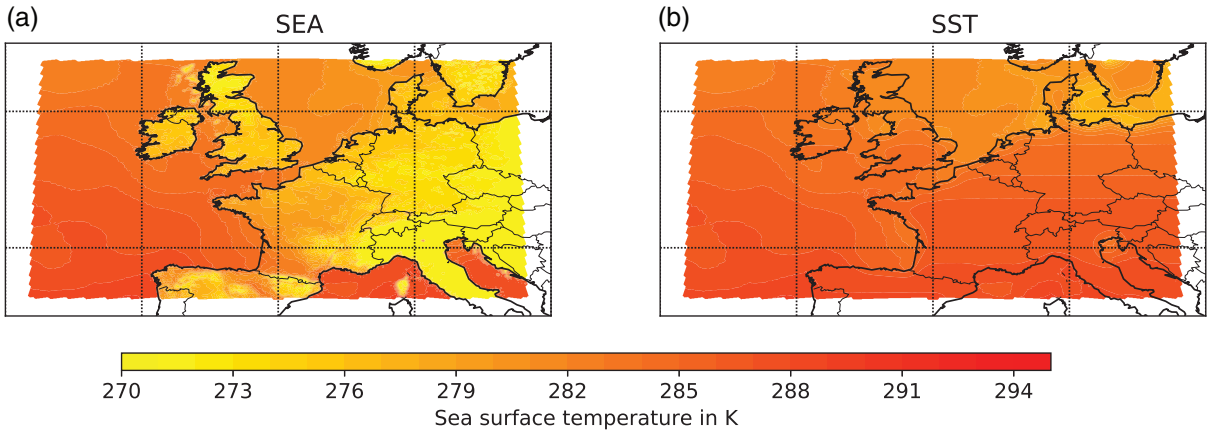

FIGURE 2 Sea-surface temperature of (a) SEA simulation, where it is taken from the initial land surface temperature of REF and FLAT, and (b) SST simulations, where it is interpolated and extrapolated from adjacent seas by solving Poisson's equation using zonal averages as initial guess

TABLE 1 Configuration of ICON-LAM simulations: name, horizontal grid spacing Δx in km and use of parametrization for deep convection; scores are given as spatial mean error *ME*, root mean square error *RMSE* and correlation coefficient *R* of simulated maximum gust speed in 10 m in $\mathrm{m \cdot s^{-1}}$ compared to observed maximum gust speeds from 12 January 2017, 0000 UTC to 14 January 2017, 0000 UTC. Only stations within the gust footprint south of the cyclone track (48°N to 51°N, black box in Figure 5) and $v_{\mathrm{gust}} > 25\,\mathrm{m \cdot s^{-1}}$ are considered for the calculation

Simulation	Δx in km	conv. param.	*ME* in $\mathrm{m \cdot s^{-1}}$	*RMSE* in $\mathrm{m \cdot s^{-1}}$	*R*
MIDRES	6.5	On	−2.2	1.6	0.55
REF	3.3	On	−1.9	1.6	0.60
NOPARAM	3.3	Off	−2.4	1.6	0.64
HIRES	1.6	Off	−1.5	1.6	0.64

combines first guess and analysis and results in a similar forecast in this case (see section 3.2).

For the simulations, three different horizontal grid spacings are used, namely 6.5, 3.3 and 1.6 km (Table 1), which all fulfil the criterion of a horizontal resolution of at least 10 to 12 km pointed out by previous authors (Clark *et al.*, 2005; Hewson and Neu, 2015; Clark and Gray, 2018). These are combined with either 50 or 90 levels, which translate into a vertical grid spacing between 1 and 3 km altitude of 140 to 244 m in the former case and of 88 to 136 m in the latter case. Clark *et al.* (2005) demand a ratio of 1:50 between horizontal and vertical resolution to represent an SJ with all possible contributing mechanisms in numerical simulations. For a small grid spacing of 1.6 km this would imply that the vertical resolution must not exceed 32 m. As Coronel *et al.* (2016) tested the 1:50 slope for their 4 km resolution, that is, 80 m vertical spacing, and found no significant improvement besides more noise, this criterion is assumed unimportant at such high resolutions. For better comparison, the analysis of the computed simulations is done on a common grid with a grid spacing of 6.5 km, where higher-resolution simulations are interpolated using first-order conservative remapping.

The ICON model includes several physical parametrizations. The cloud microphysics parametrization is based on a single-moment scheme from Doms *et al.* (2011). Prognostic turbulent kinetic energy from the Consortium for Small-scale Modelling (COSMO) model is used for turbulent transfer (Raschendorfer, 2001). Combined cloud microphysics, convection and turbulence information for the cloud cover, that is, ice and water content, is given to the radiation parametrization, which is based on the Rapid Radiative Transfer Model (RRTM) by Mlawer *et al.* (1997). The convection parametrization is based on Tiedtke (1989) and Bechtold *et al.* (2008) and is used for both deep and shallow convection. When activated for deep convection, the parametrization can produce precipitation but also contribute to wind gusts through conversion from convective available potential energy and transport of momentum from higher levels in the gust parametrization (Schultz, 2008). While shallow convection is parametrized in all simulations, deep convection is parametrized in the simulation with 6.5 km grid spacing (hereafter MIDRES) but explicitly represented in the 1.6 km simulation (hereafter HIRES). Two separate simulations are run with 3.3 km grid spacing to further test the sensitivity to the representation of deep convection, one with and one without parametrization (hereafter REF and NOPARAM; see Table 1).

Additional sensitivity experiments are conducted to investigate the influence of topography on the SJ dynamics and gust formation. For a better comparison with REF, all are run with 3.3 km grid spacing, 90 vertical levels and parametrized deep convection (Table 1). Firstly, the terrain height is set to zero over the whole model domain in simulation FLAT, without changing surface temperature. This removes the barrier of the Alps between the Atlantic and the Mediterranean as well as lower mountain ranges such as the Vosges and Black Forest along the track of the storm (Figure 1a). Secondly, the land surface is additionally replaced by sea over the now flat domain in simulation SEA. This impacts all surface properties and the surface roughness in particular, which is lowered and thus allows stronger boundary-layer winds and near-surface gusts. However, the sea-surface temperature over the removed land masses is inherited from the corresponding soil temperature and results in unrealistically low values, where high mountains were removed in particular (Figure 2a). Therefore, a third sensitivity experiment (simulation SST) is conducted where the sea-surface temperature over removed land masses is interpolated and extrapolated from the adjacent water bodies (Figure 2b). This is done by solving Poisson's equation using zonal averages as initial guess, which results in a mostly meridional gradient over the continent with smooth transitions near the coasts.

Changing the topography creates an initial shock in these sensitivity experiments. When the orography is removed, initial conditions from ICON-EU are extended down to mean sea level by shifting the boundary layer and extrapolating the free troposphere. This often results in temperature and moisture anomalies over previous mountain ranges compared to their surroundings. Furthermore, increasing the sea-surface temperature in the SST simulation induces a sudden warming of the surface layer. This may create local instabilities and can be an issue when assessing the impact of topography on summer convection in a weak synoptic flow (e.g. Schneider *et al.*, 2018). However, the fast large-scale background flow associated with *Egon* quickly ventilates the model and the relatively low sea-surface temperature in winter prevents spontaneous convective activity. For each sensitivity experiment we verified that local abnormalities resulting from changes in initial conditions do not last for more than a few hours and thus vanish before cyclogenesis occurs.

2.3 | Lagrangian trajectories

Lagrangian trajectories have often been the most important tool for a definitive SJ identification in recent case-studies (e.g. Gray *et al.*, 2011; Baker *et al.*, 2014; Martínez-Alvarado *et al.*, 2014; Schultz and Browning, 2017; Volonté *et al.*, 2018). For the calculation of trajectories, LAGRANTO (LAGRangian ANalysis TOol) is used here (Wernli and Davies, 1997; Sprenger and Wernli, 2015). Volonté *et al.* (2018) stated a significant improvement in variables such as wet-bulb potential temperature θ_W between hourly and more frequent input data from a deviation of 2 to 3 K to nearly constant behaviour. Therefore, trajectories are computed here both with a frequency of 1 h (hereafter REF60) and 15 min (REF).

To calculate trajectories with LAGRANTO, starting positions need to be defined. As in previous studies, points were chosen horizontally where the 850 hPa wind speed exceeds a certain threshold and are then extended to a vertical layer from 900 to 800 hPa. For case-studies over the ocean, it is safe to assume that this layer is representative of the strongest winds. In the case of *Egon*, however, orography may affect winds, and thus the time of most intense winds at 850 hPa is not necessarily the moment when the SJ or CJ is the strongest. For that reason, several starting points were selected. From a given starting time, trajectories were computed backwards until 12 January 2017, 1200 UTC and forwards until 13 January 2017, 0600 UTC. The calculated trajectories are based on wind speed as the sole condition. To distinguish SJ and CJ, the fundamental definition of an SJ describing a descending airstream is used as a second criterion. The thresholds differ during the analysis and are described in the corresponding sections.

2.4 | Three-dimensional visualisation

Met.3D is a three-dimensional visualisation open-source software by Rautenhaus *et al.* (2015). It was initially developed for the Ensemble Prediction System from the European Centre for Medium-Range Weather Forecasts to support weather forecasting during aircraft-based atmospheric field campaigns. Developed further within the Transregional Collaborative Research Centers "Waves to Weather," it can now also handle different datasets, horizontal grids and vertical coordinates. One of the advantages this tool brings is its interactiveness. Besides horizontal and vertical cross-sections, one can illustrate isosurfaces, for example, of a certain wind speed. Furthermore, the prior mentioned trajectories can be visualised in three dimensions and this capability is exploited here to illustrate airflows within windstorm *Egon*.

2.5 | Identification of mesoscale instabilities

In a steady-state environment several mesoscale instabilities are defined for vertical displacements, such as conditional instability (CI, moist Brunt–Väisälä frequency $N_m^2 < 0$), and for horizontal displacements, such as inertial instability (II, vertical component of absolute vorticity $\zeta_z < 0$). Furthermore, a parcel can be stable to horizontal and vertical displacements, but unstable to slantwise displacements, as in the case of symmetric instability (SI, potential vorticity $PV < 0$) and CSI.

Note that mesoscale instabilities should be interpreted with caution, because they are based on the parcel method. Strictly speaking they are only defined in a steady-state environment and this is obviously not the case within a storm like *Egon*, which is explosively developing and where air moves quickly. A small displacement thus does not necessarily result in a definite state of (in-)stability.

Following previous literature the contribution of CSI release is investigated (e.g. Parton *et al.*, 2009; Gray *et al.*, 2011; Baker *et al.*, 2014; Martínez-Alvarado *et al.*, 2014) along with the contribution of CI, II and SI, which can also contribute to SJ strengthening (Volonté *et al.*, 2018). For that purpose, the fraction of trajectories satisfying certain criteria is detected to indicate whether CSI or another instability takes place. Firstly, negative values of ζ_z and N_m^2 indicate II and CI, respectively, which by definition exclude CSI. Secondly, negative values of saturated moist potential vorticity

$$MPV^* = \frac{1}{\rho} \cdot \zeta_a \cdot \nabla_p \theta_E^*, \quad (1)$$

where ρ is the air density, ζ_a is the absolute vorticity and θ_E^* is the saturated equivalent potential temperature, are a necessary condition for CSI. Thirdly, values of relative humidity need to exceed 90% for CSI. Finally, stable conditions are thus defined for simultaneous positive values of ζ_z, PV, N_m^2 and MPV^*.

3 | SYNOPTIC EVOLUTION AND GUST FOOTPRINT

3.1 | Observations and analysis data

Early in January 2017 the weather over Europe was dominated by high-pressure conditions and cold temperatures. This changed on 10 and 11 January, when the low-pressure systems *Caius* and *Dieter* formed a strong frontal zone and brought moister and warmer air towards Europe. These two lows were located over Scandinavia when *Egon* formed as a typical secondary cyclone (Parker, 1998) along the pre-existing cold front of storm *Dieter* about 1,500 km west of France in the night to 12 January (not shown). At noon on 12 January, *Egon* had already formed a pronounced frontal wave and its centre was located at the southwestern coast of England with a pressure minimum below 1,008 hPa (see track and core pressure in Figure 1a). The cyclone still had access to warm and moist air over the Bay of Biscay (Figure 3a). The storm then developed rapidly into an intense cyclone while crossing the English Channel, with a pressure drop of 28 hPa in just 15 h (Figure 1a). This pressure drop largely exceeds the criteria for explosive cyclogenesis after Sanders and Gyakum (1980), that is, at least 1 hPa·h^{-1} for 24 h at a latitude of 60°N. One possible factor for the explosive cyclogenesis was a dry intrusion already present at the beginning of the evolution (not shown). Reaching France around 1800 UTC (Figure 1a) the

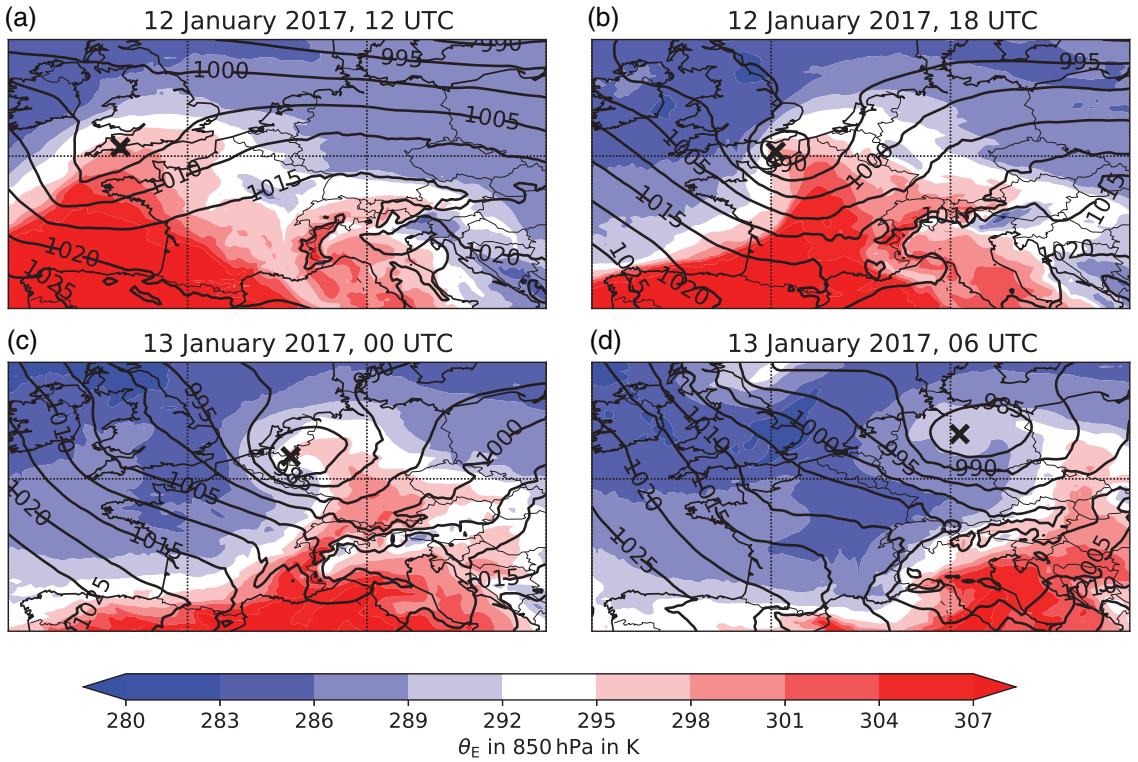

FIGURE 3 Equivalent potential temperature θ_E at 850 hPa and mean sea-surface pressure in the ICON analysis at (a) 1200 UTC and (b) 1800 UTC on 12 January and (c) 0000 UTC and (d) 0600 UTC on 13 January 2017. The cyclone centre of windstorm *Egon* is marked by the black crosses

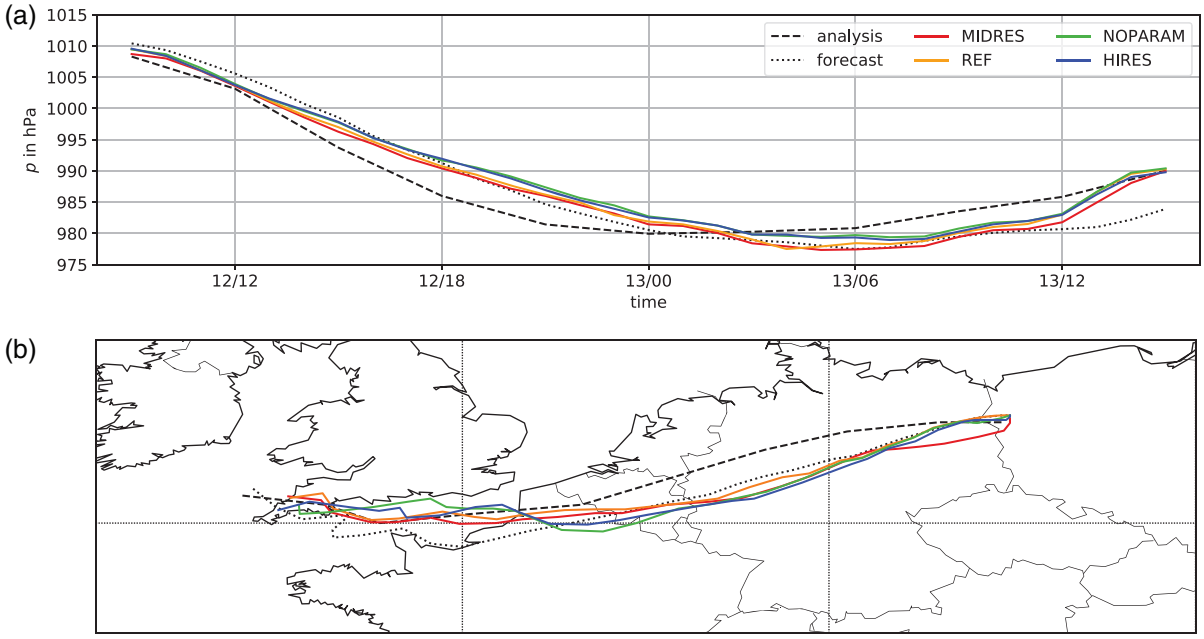

FIGURE 4 Comparison of simulations REF, MIDRES, HIRES and NOPARAM (solid lines) with the ICON analysis (dashed line) and ICON forecast (dotted line) from 12 January 2017, 0900 UTC to 13 January 2017, 1400 UTC for (a) core pressure and (b) storm track

cyclone developed further and a frontal fracture appeared shortly after, indicating stage II of a Shapiro–Keyser cyclone (Figure 3b). With the cyclone now over land, values of θ_E began to decrease. The cyclone track crossed the north of France, Belgium and the Netherlands, and reached Germany shortly after midnight on 13 January, when the ICON analysis shows the lowest pressure during the evolution with 979.9 hPa near Weert, Netherlands (Figure 1a). Figure 3c indicates that the Alps blocked warm and moist air from the Mediterranean Sea leading to a further decrease in θ_E. The cyclone showed a developing T-bone structure, which characterises stage III in the life cycle of a Shapiro–Keyser cyclone. The core pressure remained around 980 hPa for the next few hours while tracking eastwards over Germany (Figure 1a). This is consistent with station observations. A minimum pressure of 979.8 hPa was measured at 0400 UTC in Wernigerode, Germany. At 0600 UTC warm air was secluded by the bent-back front, which indicates stage IV of a Shapiro–Keyser cyclone (Figure 3d), and the cyclone began to weaken. The centre of *Egon* eventually reached Poland at noon of 13 January with a pressure minimum of 985 hPa (Figure 1a).

Egon's track over Europe left behind a footprint of strong surface gusts south of the centre's track from northern France to eastern Germany (Figure 1). The highest gust speeds were measured over Germany at peaks of two low-mountain ranges: Weinbiet close to the French border (554 m) with 41 m·s^{-1} and Fichtelberg close to the Czech border (1,215 m) with 42 m·s^{-1}. Scaling the gust speeds over Germany by the local 98th climatological percentile to make different stations more comparable reveals an even more distinct footprint stretching from Luxembourg to the Czech border (Figure S1).

3.2 | Model simulations

Figure 4 shows the time evolution of the core pressure and the associated storm track comparing simulations REF, MIDRES, NOPARAM and HIRES with the ICON operational forecast initialised at 0000 UTC on 12 January 2017 and the ICON analysis. All simulations have a similar core pressure evolution and track, and are also similar to the ICON forecast. The standard deviation *SD* of core pressure values between simulations varies between 0.14 and 1.1 hPa. However, all simulations deepen slower than the analysis, hence reach the minimum with a delay of a few hours, and the pressure increases again later (Figure 4a). The biggest deviations happen on 12 January, 2000 UTC and on 13 January, 0800 UTC with an average of −5.4 and +3.6 hPa, respectively. In comparison to the pressure drop of ∼28 hPa in the analysis, the simulations exhibit a drop of ∼30 hPa. Calculated mean errors (*ME*) of pressure values over Germany are around 1.7 hPa in MIDRES and between 1.1 and 1.3 hPa in higher resolutions. Furthermore, the simulated storm track over the continent is shifted southward by up to ∼100 km compared to the analysis (Figure 4b). To ensure that this is not the consequence of using the forecast as boundary conditions, a simulation was also computed with the ICON analysis as boundary conditions but this did not result in a clear difference (not shown). Despite these small biases, the simulations depict the synoptic evolution of windstorm *Egon* satisfactorily. Simulations and analysis converge again at the end of the evolution, when the cyclone is filling (Figure 4).

Consistent with the observations (Figure 1a), all simulations show a footprint of high gust speeds over

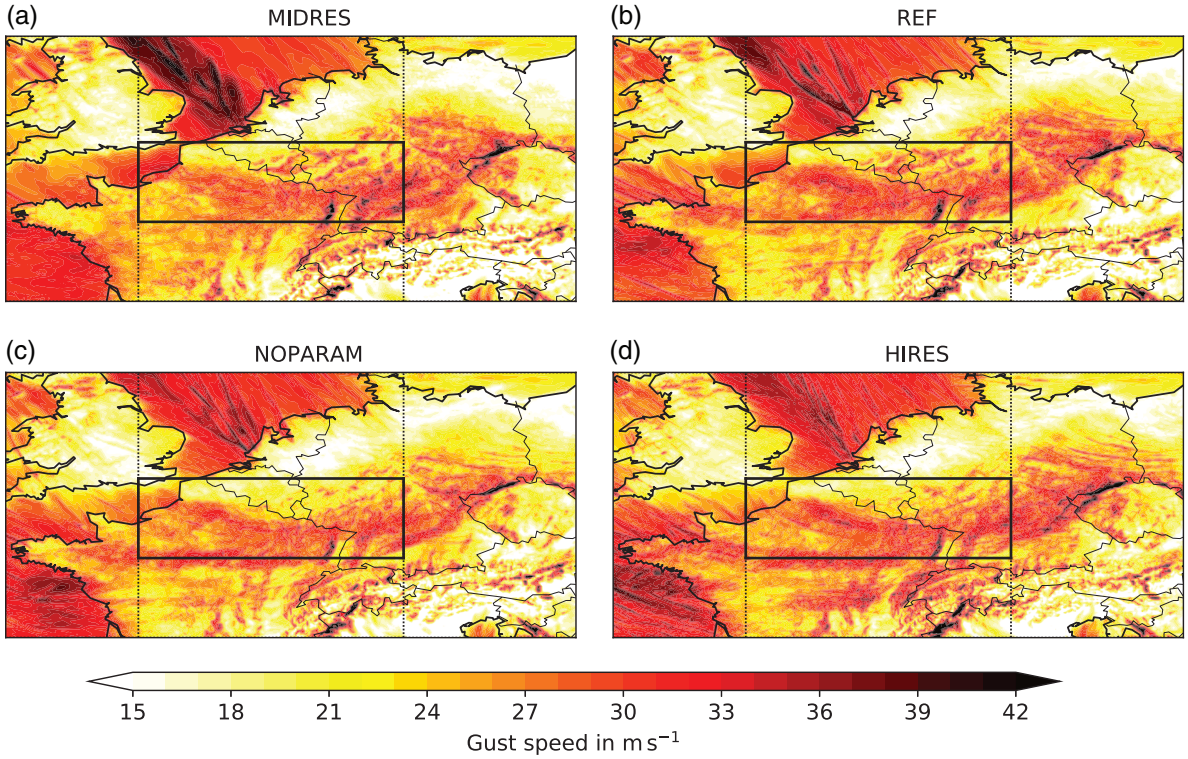

FIGURE 5 Simulated maximum 10 m gust speeds from 12 January 2017, 0000 UTC to 14 January 2017, 0000 UTC in simulations (a) MIDRES, (b) REF, (c) NOPARAM and (d) HIRES. The black box indicates the area used for score calculations in Table 1

northern France extending over central Germany towards Poland (Figure 5). High gust speeds are also found over the North Sea but are due to another storm and are not further discussed here. The corresponding footprints in wind speeds at 850 hPa are structurally similar (not shown). While the gust footprint is clearly visible in MIDRES, it gets even more pronounced with increasing resolution (Figure 5). The influence of orography can be seen in all simulations, for example, over the Vosges Mountains and the Black Forest near the French-German border and the Ore Mountains at the Czech-German border, where high gusts are simulated. Comparing the footprint with the evolution of *Egon* suggests that the high gusts over France, Belgium, Luxembourg and western Germany are caused by an SJ. For this region (black rectangle in Figure 5) the spatial mean error *ME*, root mean square error *RMSE* and correlation coefficient *R* are calculated for all simulations (Table 1). No clear differences in gust speeds are found between 50 and 90 vertical levels (not shown), such that simulations with 50 levels are not considered in the following analysis. The *ME* indicates that all simulations underestimate the strength of the gust footprint (Table 1). This is mainly due to the southward shift in the simulated track (Figure 4). Increasing resolution improves scores of *ME* and *R* but only slightly and does not affect *RMSE* (Table 1). For computational constraints, the 3.3 km grid spacing is thus chosen for the following sensitivity tests.

Concerning the representation of convection with 3.3 km grid spacing, *ME* and *R* show contrasting sensitivity (Table 1). In NOPARAM the footprint over northern France is weaker than in all other simulations and also compared to observations, which increases the negative bias (Figures 1a and 5). In contrast, a second pronounced footprint in France, south of the first one, appears when the convection parametrization is turned off, that is, in simulations NOPARAM and HIRES. Comparing NOPARAM with observations suggests an overestimation of gust speeds in this latter area (Figures 1a and 5). The new footprint is located at the edge of the southern area for which *ME*, *RMSE* and *R* are calculated and therefore also influences the scores (Table 1). The reason why this second wind maximum only occurs in simulations without convection parametrization is unclear. Precipitation is mainly caused by the bent-back front and therefore remains to the north of the main gust footprint with weak differences between REF and NOPARAM (not shown). We assume that small-scale convection, for example, behind the cold front, may partially remain a subgrid-scale process at a 3.3 km grid spacing and decided to use the simulation with convection parametrization as reference (REF).

4 | ANALYSIS OF STING JET CHARACTERISTICS

This section begins with a discussion of low-level jets, SJ and CJ trajectories and mesoscale instabilities in the REF simulation, closely following methods proposed in previous

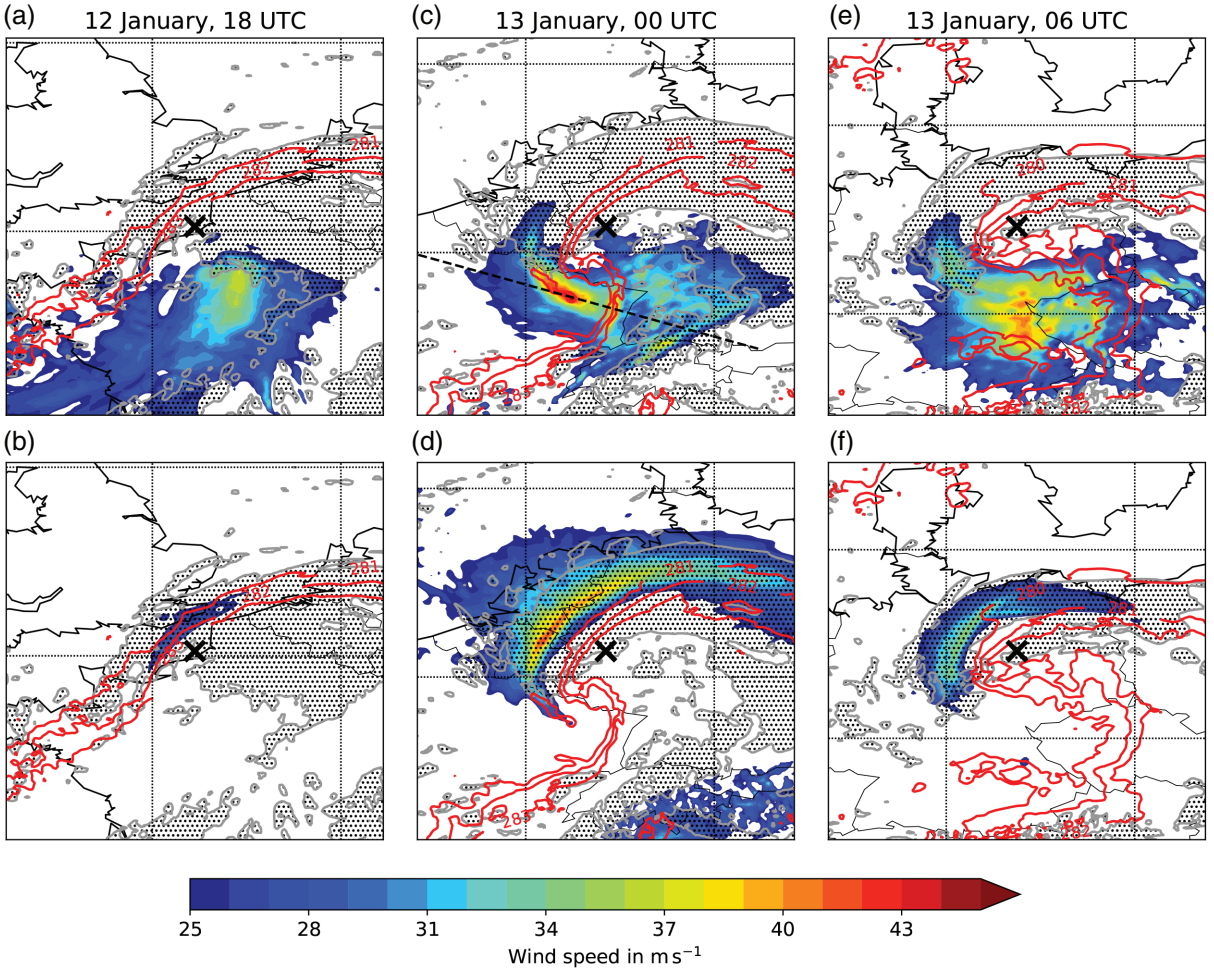

FIGURE 6 (a,c,e) Earth-relative and (b,d,f) system-relative wind speed at 850 hPa (shaded) in the REF simulation at (a,b) 1800 UTC on 12 January, (c,d) 0000 UTC and (e,f) 0600 UTC on 13 January 2017. Also shown are the cloud cover >80% (dotted area), three equivalent potential temperature contours at 850 hPa representing the frontal zone (red contours) and the cyclone centre (cross). The dashed black line in (c) indicates the location of the vertical cross-section in Figure 7

literature, especially in Volonté *et al.* (2018). The second part then focuses on the sensitivity of the results to model configuration (resolution, convective parametrization) and trajectory computation and identification.

4.1 | Detailed analysis of the REF simulation

4.1.1 | Low-level jets

The wind speed within a cyclone highlights different airflows depending on which reference frame is used. In particular, considering the Earth- and system-relative wind speed allows linking airflows to their location relative to the cyclone structure and evolution, thus helps identify wind phenomena such as conveyor belt jets and SJs. Since WJs and SJs mainly move with the cyclone, their wind speeds can be seen in an Earth-relative framework (e.g. Volonté *et al.*, 2018). In contrast, CJs wrap around the cyclone centre travelling along the bent-back front, hence against the cyclone motion, and can be first seen in the system-relative framework. When a CJ wraps around the centre at later stages, it also appears in the Earth-relative framework.

Figure 6 shows the Earth- and system-relative wind speed at 850 hPa in REF. The equivalent potential temperature θ_E at 850 hPa represents the frontal zone (red contours). At 1800 UTC on 12 January strong Earth-relative wind speeds of $\sim$35 m·s^{-1} can be seen to the southeast of the cyclone centre and to the east of the θ_E contours, which suggest that they are mainly caused by the WJ ahead of the cold front (Figure 6a). So far, only a thin area of system-relative wind speeds around 26 m·s^{-1} occurs to the northwest of the cyclone centre (Figure 6b). With increasing time, wind speeds east of the front slightly weaken in the Earth-relative framework. Instead a new area of strong winds exceeding 42 m·s^{-1} appears southwest of the centre at 0000 UTC on 13 February (Figure 6c). It is located where the frontal-fracture region occurs, which supports the SJ hypothesis. A striking feature is the local maximum in θ_E co-located with the strongest winds. In order to further investigate this, Figure 7 shows a vertical cross-section through the region of highest winds at 850 hPa stretching

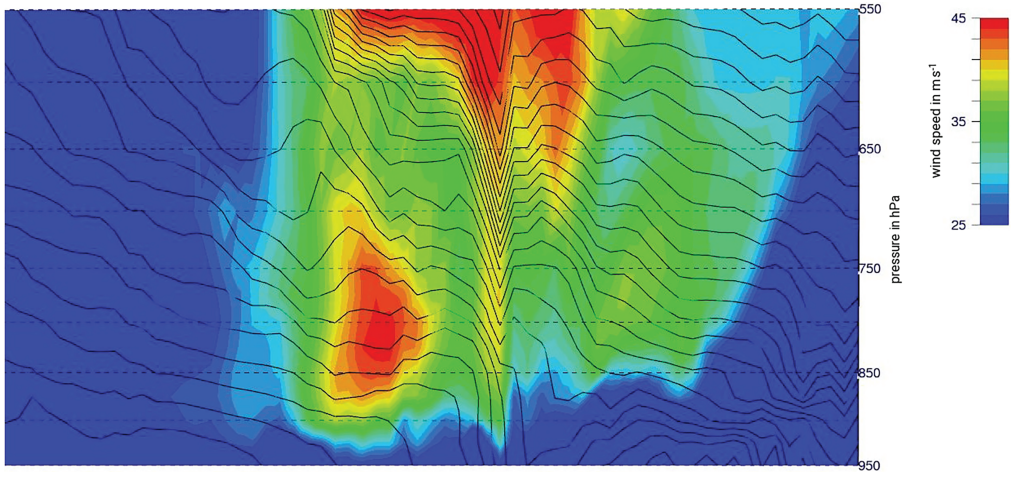

FIGURE 7 Vertical cross-section of Earth-relative wind speed (shaded) and equivalent potential temperature (line contours) in the REF simulation at 0000 UTC on 13 January 2017. The location of the cross-section can be seen in Figure 6c. Note that all wind speeds smaller than 25 $m \cdot s^{-1}$ are shaded blue to emphasise the main high-wind areas. Image produced using Met.3D

from northeastern France to the German-Austrian border (Figure 6c). The local maximum in θ_E at 850 hPa appears to be connected to a much larger-amplitude wave at higher levels peaking at around 600 hPa a little farther to the west than the low-level wind maximum. This slanted structure suggests a folding of θ_E lines through the release of mesoscale instabilities in the SJ region. Furthermore, a sharp buckling of θ_E and wind contours is evident east of the low-level wind maximum and above the interception with the frontal zone at 850 hPa (Figure 6c). This vertical structure is consistent with the presence of CI (not shown) and indicates active convection. In the system-relative framework at this time (Figure 6d), a strengthening of wind speed reaching ~40 $m \cdot s^{-1}$ can be seen. The strongest winds occur along the bent-back front and wrap around the cyclone centre, hence are likely caused by a CJ.

Until 0600 UTC the maximum of Earth-relative wind speed moves eastward towards the Czech-German border and grows in spatial extent. However, the highest speeds decrease to below 40 $m \cdot s^{-1}$ (Figure 6e). Strong winds attributed to a CJ wrap around the centre and into the direction of the cyclone motion. Therefore, the winds are seen in both system- and Earth-relative wind speed, though weakening in the system-relative framework as well (Figure 6e,f). Contours of θ_E suggest that the cyclone is at stage IV of the Shapiro–Keyser life cycle, when an SJ has typically disappeared. These results suggest that strong winds are caused by both SJ and CJ for several hours but do not provide a clear separation between the two air streams, which is presented in section 4.1.2.

4.1.2 | Trajectory analysis

As mentioned above, trajectories are crucial to confirm the presence of an SJ. For a detailed analysis of REF, a wind speed threshold of 37 $m \cdot s^{-1}$ and a pressure increase by at least 150 hPa in 8 h until the starting time of the computation of the trajectories are chosen. CJ trajectories are also classified with the same wind speed threshold and a second condition, $p > 800$ hPa, determining that the airflow remains at low levels.

Since orography can contribute to the highest gust speeds, it is not clear when the SJ occurred exactly. Looking at the evolution of Earth-relative wind speed as in Figure 6a,c,e and times in between suggests the presence of the SJ for several hours. Therefore, backward and forward trajectories are calculated for hourly starting times from 12 January, 2100 UTC to 13 January, 0600 UTC. The number of trajectories satisfying the SJ conditions increases with time from just 5 trajectories at 2200 UTC to 206 trajectories at 0300 UTC and decreases rapidly to just 1 trajectory at 0500 UTC. Independently of the starting time, the parcels undergo a similar path: starting over the United Kingdom, travelling over northern France and southern Germany following the bent-back front into the frontal-fracture region (Figure S2a,b). All trajectories originate from levels between 700 and 600 hPa, hence satisfy the SJ definition. Note that trajectories that are started later, hence reaching the boundary layer later, originate on average from higher levels (Figure S2c). Moreover, they all accelerate during the descent, which satisfies another SJ characteristic (Figure S2d).

For the following, the focus is put on trajectories started at 0200 UTC on 13 January, which produce the longest period of high wind speeds. In total, 192 trajectories satisfy the SJ criteria at this starting time. Figure 8 illustrates all trajectories that match the above criteria. It shows two clearly distinct jets in both Earth- and system-relative frameworks and thus confirms the presence of both SJ and CJ within the structure of windstorm *Egon*. While the SJ originates from southern Great Britain, the CJ originates further eastward (Figure 8a). The two come closer over the continent,

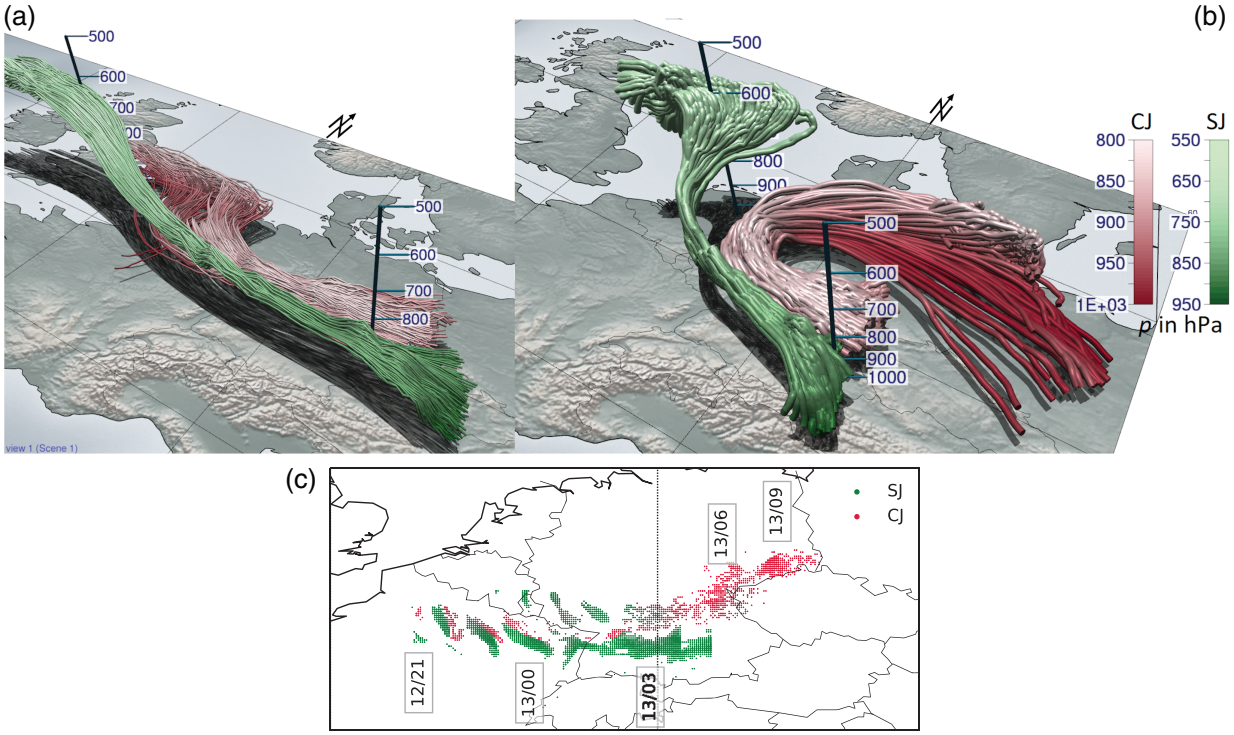

FIGURE 8 Three-dimensional visualisation of sting jet (SJ; green) and cold jet (CJ; red) trajectories started at 0200 UTC on 13 January in (a) an Earth- and (b) a system-relative framework in the REF simulation. Shading indicates altitude in hPa. Imagery produced using Met.3D. (c) Starting points for the computation of trajectories at 850 hPa from 2100 UTC on 12 January to 1100 UTC on 13 January 2017 in hourly increments. Green points match SJ and red points CJ selection criteria. Both SJ and CJ trajectories must exceed a wind speed of 37 $m \cdot s^{-1}$ at starting time. The pressure of SJ trajectories must decrease by at least 150 hPa in 8 h, while it has to remain below 800 hPa for CJ trajectories at all times

where they partly merge and travel alongside each other over southern and central Germany south of the cyclone centre. Adopting a system-relative framework, Figure 8b illustrates that while the CJ follows the bent-back front at all times, the SJ originates from more western areas before joining the motion of the bent-back front.

The additional starting times allow relating identified trajectories with resulting winds. Comparing both SJ and CJ trajectories in Figure 8a with the footprint of REF in Figure 5b suggests that high gusts over northern France and southern Germany are mainly caused by the SJ, while high gusts over central Germany, hence north of the SJ, are associated with the CJ. Lagrangian trajectories cannot uniquely determine the origin of gusts, because they do not follow boundary-layer turbulence. Instead, strong winds at 850 hPa are objectively assigned to either SJ or CJ with the assumption that they result in strong gusts, although the processes that drive downward mixing are influenced by stability and may differ between SJ and CJ. Combining trajectories from different starting times emphasises a common SJ and CJ footprint over northern France initially on 12 January, 2100 UTC, which separates into two distinct branches on 13 January (Figure 8c). As expected, the southern branch is issued from the SJ footprint, while the northern branch is issued from the CJ footprint that lasts longer and extends further eastward. This largely confirms the hypothesis based on Earth- and system-relative winds in Figure 6 but also highlights that disentangling SJ and CJ contributions is far from obvious.

SJ trajectories started at 0200 UTC on 13 January mainly originate from 600 to 700 hPa (Figure 8a). The descent starts slowly from around 1530 UTC to 1930 UTC with ~70 hPa during these 4 h. Afterwards, the descent accelerates. Until 0400 UTC the air parcels move almost 200 hPa downwards, some even reaching below 850 hPa. They then rise again by 50 hPa when reaching the Bohemian Forest at the German-Czech border (not shown). The rate of pressure increase between 1900 UTC and 0600 UTC is ~22 $hPa \cdot h^{-1}$ on average.

The Earth-relative wind speed accelerates from 20 to 40 $m \cdot s^{-1}$ between 2000 UTC and 0030 UTC (Figure 9a). The wind speed reaches a plateau of high winds between around 0030 UTC and 0230 UTC and decreases afterwards. A plateau is also reached by trajectories started at different times (Figure S2d), which indicates both that the surface footprint is caused by newly descending air and that a descended flow can cause strong gusts over several hours. In the system-relative framework, Figure 9b shows that the wind speed already starts accelerating at 1800 UTC to a maximum of ~20 to 25 $m \cdot s^{-1}$ at around 0100 UTC. Since the acceleration happens in both frameworks and with a deviation of only ~2 $m \cdot s^{-1}$, it is mainly due to the air entering a region of enhanced wind speed, as

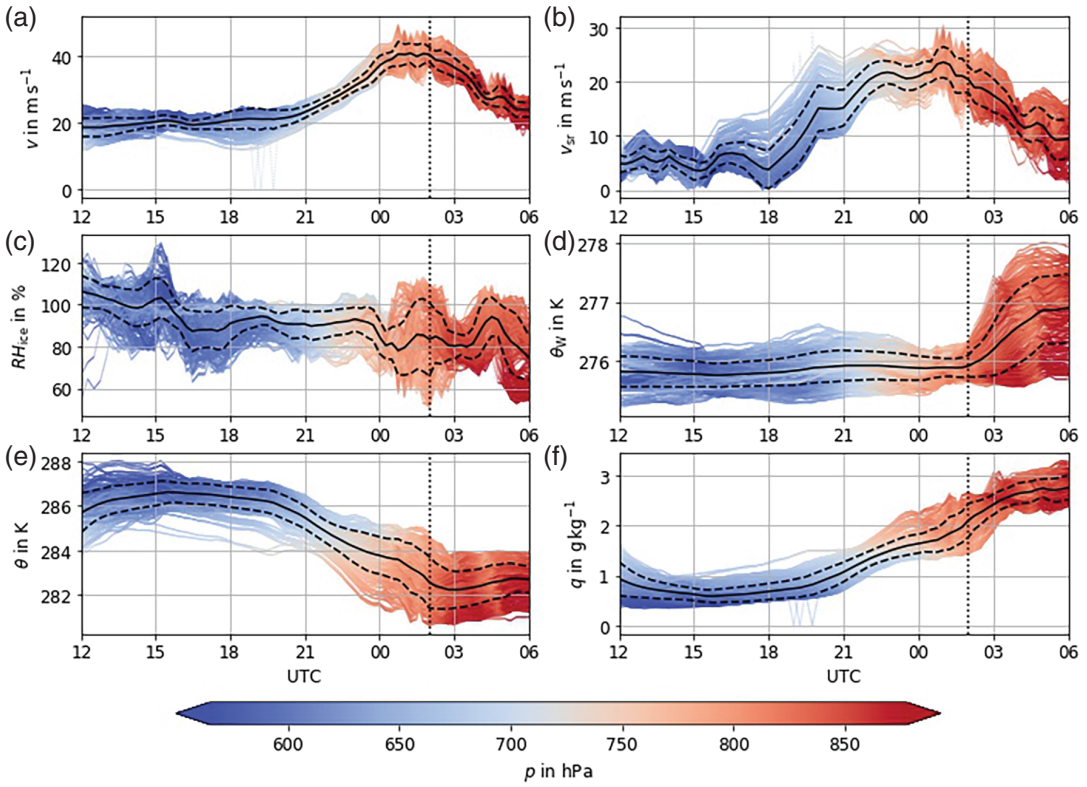

FIGURE 9 SJ trajectories in the REF simulation: (a) Earth-relative wind speed, (b) system-relative wind speed, (c) relative humidity with respect to ice, (d) wet-bulb potential temperature, (e) potential temperature and (f) specific humidity. Start time is at 13 January 2017, 0200 UTC (dotted line), calculated forwards to 0600 UTC, backwards to 12 January 2017, 1200 UTC. Shading indicates pressure along trajectories, solid lines the mean of trajectories and dashed lines the *SD*

expected for an SJ, rather than turning to the direction of the cyclone motion, as expected for a CJ. The fact that the trajectories descend into the frontal-fracture region (not shown) while accelerating is clear evidence for the presence of an SJ during the evolution of windstorm *Egon*.

With the beginning of the descent shortly after 1500 UTC, the trajectories show a drying by ∼15% RH_{ice} in 2.5 h (Figure 9c). In contrast to other case-studies (e.g. Parton *et al.*, 2009; Baker *et al.*, 2014; Volonté *et al.*, 2018), which showed further drying to below 50%, RH_{ice} remains stable at ∼90% almost until midnight. Only then does it decrease by a further 15% in 1.5 h but remains above 80% on average until the time of maximum intensity, before fluctuating later with an increase in *SD*. Consistent with this high humidity, cloud cover values suggest that the cloud base in the SJ area was as low as 900 hPa, hence that the SJ only left the cloud head shortly before it reached low levels and thus did not have time to dry out.

Figure 9d further shows that values of wet-bulb potential temperature θ_{W} are nearly constant during most of the descent, whereby a third characteristic of an SJ mentioned in Baker *et al.* (2014) is matched (see section 1). At around 0130 UTC, when most trajectories are close to 800 hPa, θ_{W} increases rapidly by up to 2 K. This increase is likely caused by turbulent mixing within the boundary layer. Additionally, the specific humidity q increases on average by 1.5 g·kg^{-1} between 1500 UTC and 0200 UTC (Figure 9f) and the potential temperature θ decreases by almost 4 K at the same times (Figure 9e). Together, the behaviour in θ_{W}, q and θ suggests evaporative cooling (Clark *et al.*, 2005). Both the increase in q and the decrease in θ show that evaporative cooling is more than twice as strong as in previous cases (e.g. Volonté *et al.*, 2018). This strong evaporative cooling explains the missing drying in RH_{ice}.

Altogether the presence of the SJ within storm *Egon* is verified by several parameters along trajectories started at 0200 UTC on 13 January. First, an airstream originating from mid-levels and descending into the frontal-fracture region is evident. Furthermore, the acceleration in both Earth- and system-relative wind speed, as well as the descent on surfaces of constant θ_{W}, are consistent with characteristics described in Baker *et al.* (2014). However, a fourth characteristic, namely the reduction of RH_{ice}, is not confirmed here due to strong evaporative cooling.

4.1.3 | Mesoscale instabilities

Trajectories further allow investigating the reasons for acceleration during the SJ descent. Figure 10 shows the proportion of trajectories satisfying criteria of CSI, II, SI, CI and

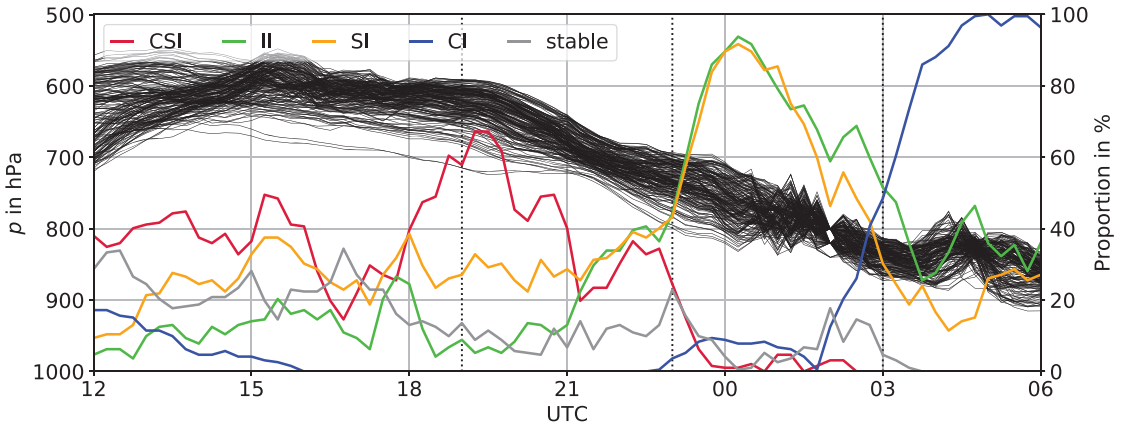

FIGURE 10 Proportion of SJ trajectories satisfying criteria of CSI, II, SI, CI and stability (see section 2) and pressure of trajectories (black curves) over time in the REF simulation. Trajectories are started at 13 January 2017, 0200 UTC calculated backwards to 1200 UTC and forwards to 0600 UTC. The dotted lines indicate the times shown in spatial maps of mesoscale instabilities in Figure 11

absence of any instability, that is, stability. The number of trajectories satisfying CSI criteria increases during the slow descent. When the parcels reach the onset of stronger descent at around 1930 UTC the number reaches its maximum with 66%. With the stronger descent the proportion decreases and fluctuates down to below 5% around midnight. Meanwhile, the fraction of trajectories satisfying II increases to up to 90% shortly after midnight. This is consistent with the decrease in CSI proportion, since per definition both instabilities cannot coexist (see section 2.5). Besides II, the proportion of SI also increases to ~90%. Martínez-Alvarado *et al.* (2014) suggest that CSI release causes a creasing of absolute momentum surfaces what leads to II strips and also influences the SI proportion. Furthermore, note that SI is not a conditional instability and can also occur in non-saturated environments. This is supported by the timing of occurrence of both II and SI here. After reaching their maxima at 0015 UTC, both proportions decrease again to ~20% at around 0400 UTC. The proportion of CI, which by definition cannot coexist with CSI either, also increases slightly from ~0 to 10% around 2200 UTC. This increase is too weak to play a role in the decrease of CSI proportion, which is already low by that time. At later stages, the proportion of CI increases rapidly, notably shortly before 0200 UTC, and reaches 100% at around 0530 UTC, but appears not to be released during the analysed time. As RH_{ice} is a criterion for CSI, the lower RH_{ice} after midnight (Figure 9c) also plays a minor role in the CSI decrease, besides II and CI. Interestingly, the fraction of stable trajectories never exceeds 30% during the entire descent (Figure 10).

When looking at the evolution of individual SJ trajectories, it is found that more than 99% of them encounter each type of instability at some point during the descent from 12 January, 1200 UTC until 13 January, 0600 UTC (Figure 10). The averaged time during which the trajectories satisfy a given instability criterion when they descend is (5.3 ± 2.1) h for CSI, (6.1 ± 1.9) h for II, (6.8 ± 2.1) h for SI and (4.1 ± 0.8) h for CI. These results suggest that all mesoscale instabilities contribute to the SJ acceleration. CSI appears crucial to trigger the descent in an early stage still within the cloud head while II and SI take over later during the descent with a similar contribution. This is consistent with previous cases, for example, *Tini* in February 2014 (Volonté *et al.*, 2018). CI only rises at the end of the descent, when SJ trajectories reach the boundary layer, and may thus support the downward mixing of strong winds to the surface.

The relative contributions of CSI, II, SI and CI are further illustrated spatially in Figure 11 as snapshots of all mesoscale instabilities and their combinations at three representative times and heights during the descent (see dotted vertical lines in Figure 10). During the CSI peak on 12 January, 1900 UTC, SJ trajectories at 650 hPa are co-located with banded structures of mixed CSI and SI as well as II within the frontal zone (Figure 11a). When the contribution of II and SI starts increasing 4 h later at 2300 UTC, SJ trajectories descend faster and wrap around the cyclone centre following mesoscale structures of mixed CSI and SI into the frontal-fracture region at 700 hPa, while new structures of mixed II and CI are emerging (Figure 11b). Finally, when CI takes over on 13 January, 0300 UTC, SJ trajectories have left the bent-back front and approach the boundary layer at 850 hPa, where the different instabilities are less clearly organised (Figure 11c). These maps reveal that CSI, SI and II are often present simultaneously, although their contribution to SJ acceleration vary during different phases of the cyclone evolution as shown in Figure 10.

4.2 | Sensitivity to model configuration and trajectory identification

The results from trajectories can be very sensitive to model configuration, for example, horizontal resolution and convection parametrization, and trajectory computation, which

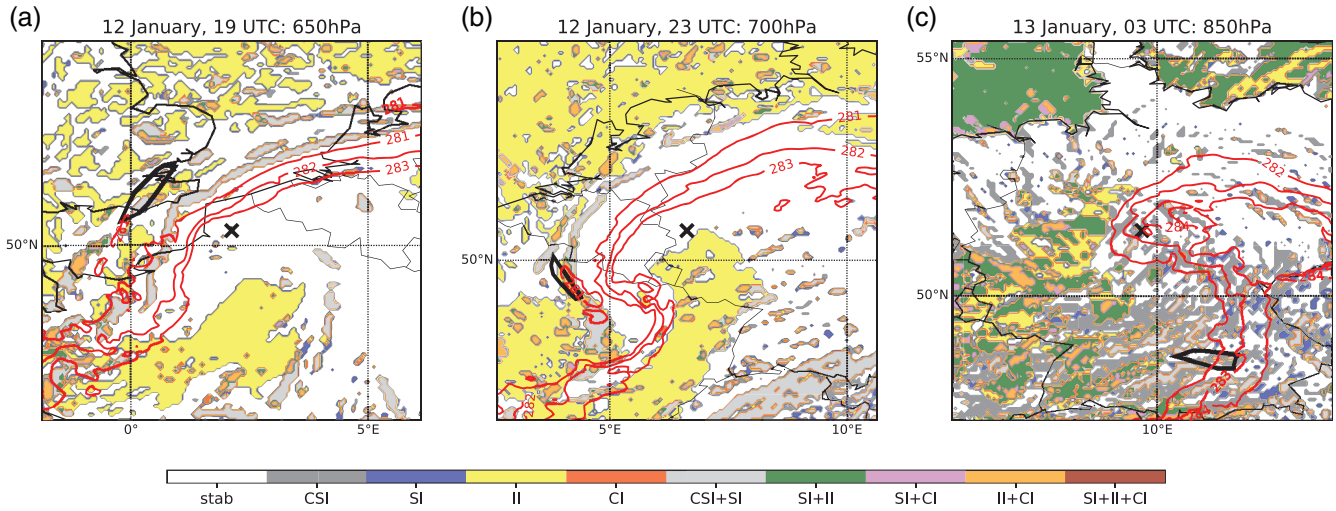

FIGURE 11 Spatial maps of CSI, II, SI, CI and their coincidence as well as stable conditions (shading; see section 2) around the cyclone centre (black cross) for (a) 650 hPa and 1900 UTC on 12 January 2017, (b) 700 hPa and 2300 UTC on 12 January 2017 and (c) 850 hPa and 0300 UTC on 13 January 2017. Three equivalent potential temperature contours at 850 hPa representing the frontal zone are indicated by red lines in analogy to Figure 6 and the area of SJ trajectories at the given level is bounded by bold black lines

are investigated here. As some model configurations show weaker winds or descent than REF, the thresholds used before are lowered to 35 $m \cdot s^{-1}$ for wind speed and 125 hPa in 8 h for pressure increase. The new thresholds yield 292 SJ trajectories started at 0200 UTC on 13 January for REF.

4.2.1 | Horizontal resolution

Since all chosen resolutions meet the criterion of a grid spacing as fine as 10 to 12 km that is needed to resolve mesoscale instabilities, it is of interest whether the enhancement of resolution on a kilometre scale strongly changes the representation of the SJ. When the thresholds mentioned above are applied, all simulations show the presence of an SJ with 258 trajectories for MIDRES but only 101 trajectories for HIRES. This indicates that the coarser simulation produces a stronger SJ here. Results are generally close for REF and MIDRES, whereas HIRES shows larger differences.

Both the Earth-relative and the system-relative path of SJ trajectories are similar at all resolutions for most of the time (Figure 12a,b). Only in HIRES it originates from ~50 hPa higher pressure than in REF and shows a slower descent between around 2200 UTC and 0100 UTC (Figure 12c). As all simulations descend to a similar level, HIRES shows the weakest descent overall. The most notable impact of resolution lies in RH_{ice}, which shows drying down to below 70% for HIRES (Figure 13a). However, these values still remain high compared to those from former case-studies. While the Earth-relative wind speed is mostly consistent between the simulations (Figure 12d), HIRES again stands out with a weaker acceleration in system-relative wind speed (Figure 12e). Although each increase in resolution leads to higher θ_W by about 1 K, all simulations show that the descent occurs with nearly constant values of θ_W (Figure 12f). Note that HIRES exhibits a weak decrease by 0.5 K between 2100 UTC and 0100 UTC. This small-amplitude variation could be caused by physical processes such as ice sublimation, but could also be related to numerical uncertainties inherent to the computation of trajectories. The consistency of constant θ_W, decrease in θ and simultaneous increase in q (Figure 12f,g,h) indicates evaporative cooling in all simulations. However, the increase in q is weakest in HIRES, which is consistent with the weaker descent mentioned above. Moreover, the increase in q is paused between 2100 UTC and 0100 UTC, corresponding to the time of small decrease in θ_W. Additionally, the decrease in θ is slightly weaker during that time, which is also consistent with the slightly decelerated descent discussed above. Altogether, it can be said that SJ trajectories do not fundamentally change when the resolution is increased at spacings of just a few kilometres. Nonetheless a clear weakening of the SJ when refining the grid spacing to 1.6 km is found particularly in values of p, v_{sr} and q.

Since a high horizontal resolution is crucial to resolve mesoscale instability, it is expected that the contribution of CSI becomes more important with increasing resolution. Indeed, the contribution of CSI becomes more salient for an increase with resolution (Figure 13c). MIDRES shows a low proportion below 20% until 1900 UTC from where it increases to over 40% at 2200 UTC, after which it gradually decreases. In contrast, HIRES trajectories reach a maximum around 1800 UTC to 2030 UTC analogous to REF with up to 80%. The proportion decreases to below 10% shortly after 2100 UTC but it increases again to a second maximum of almost 40%. Only from 0200 UTC onward the proportion vanishes and remains low. These differences in CSI contribution are mainly due to inertial stability and $MPV*$ values:

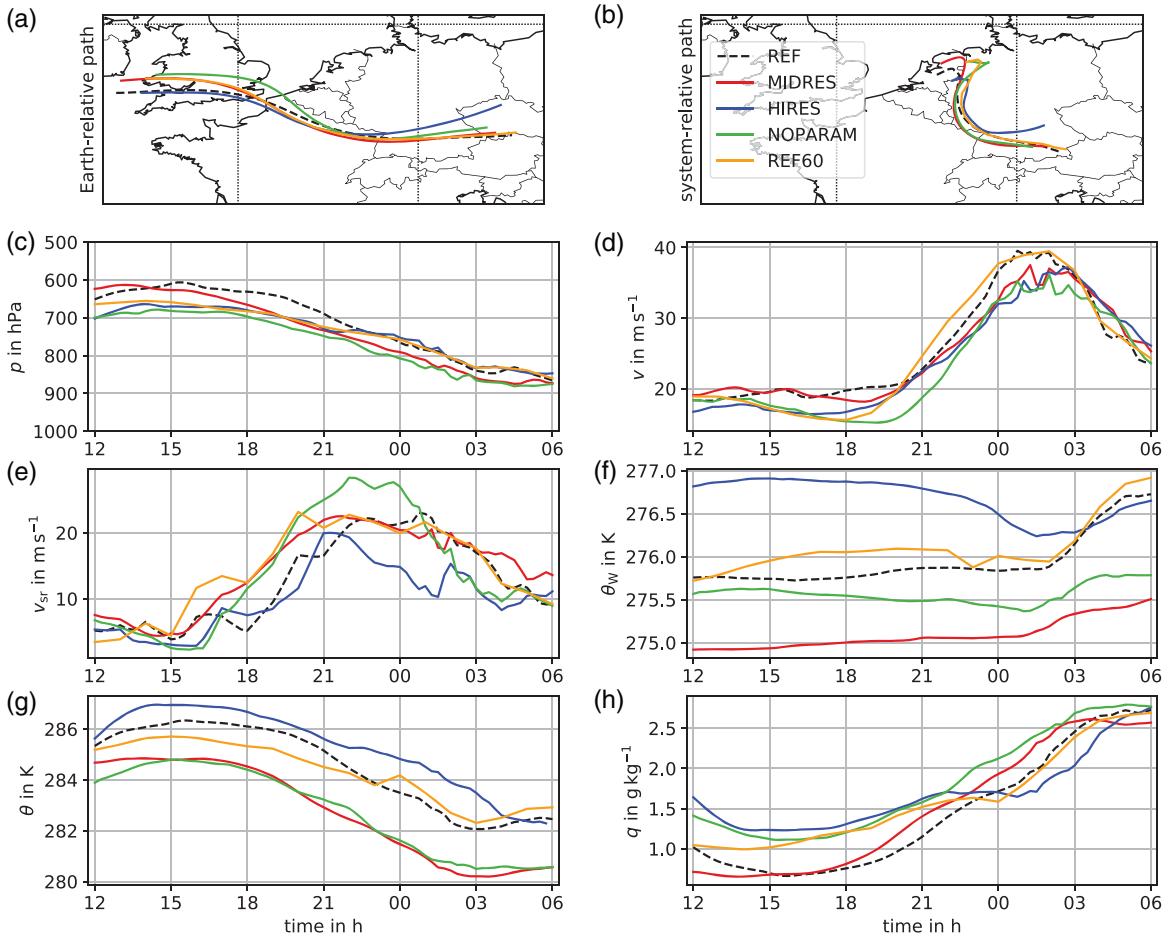

FIGURE 12 Average values along SJ trajectories for (a) Earth-relative path, (b) system-relative path, (c) pressure, (d) Earth-relative wind speed, (e) system-relative wind speed, (f) wet-bulb potential temperature, (g) potential temperature and (h) specific humidity in REF (dashed lines), MIDRES, HIRES, NOPARAM and REF60. Trajectories are started at 13 January 2017, 0200 UTC, calculated backwards to 1200 UTC and forwards to 0600 UTC. Wind speed must exceed 35 $m \cdot s^{-1}$ at starting time and pressure must decrease by 125 hPa in 8 h

while REF trajectories become inertially unstable around midnight, which leads to a decrease in CSI points, more trajectories maintain inertial stability in MIDRES and HIRES (not shown). It should be noted that *MPV* * values are close to zero, hence a small deviation can already determine (in-)stability. Furthermore, regions of negative *MPV* * and mesoscale instabilities become smaller but more with increasing the resolution (not shown). As mentioned in section 4.1.3, several instabilities can occur simultaneously and cannot always be clearly separated. Again, with the decline in CSI proportion, SI proportion is increasing in all simulations (Figure 13e) and suggests CSI release. The proportion of SI in HIRES reaches a maximum at 2300 UTC with around 55% before decreasing again when the proportion of CSI increases (Figure 13c). After 0100 UTC the proportion of CI increases in all simulations, while it is around 20% higher in HIRES than in MIDRES (not shown). This is consistent with slightly higher 10 m gust speeds in Figure 5. Despite these differences, all simulations show the presence of several mesoscale instabilities and a CSI proportion of more than 50% at some point during the descent and a decrease to zero when reaching lower levels followed by an increase of SI proportion, thus confirming the role of mesoscale instabilities in SJ acceleration.

4.2.2 | Convection parametrization

Following section 3.2, the 3.3 km simulation with convection parametrization was chosen as reference (REF). Nonetheless, trajectories are also calculated for the 3.3 km simulation without convection parametrization (NOPARAM). Consistent with the weaker SJ footprint in NOPARAM (black box in Figure 5c), only 35 trajectories satisfy the SJ criteria.

Although the system-relative path is consistent with REF (Figure 12b), NOPARAM trajectories originate further north and have a slightly more meridional component when reaching continental Europe (Figure 12a). Furthermore, while REF trajectories originate from ~600 hPa, NOPARAM trajectories start at ~680 hPa and reach 800 hPa earlier (Figure 12c). The paths from the two simulations meet shortly after reaching the continent and overall differences between both trajectory sets seem smaller over land. In particular, independent of the use or not of convection parametrization,

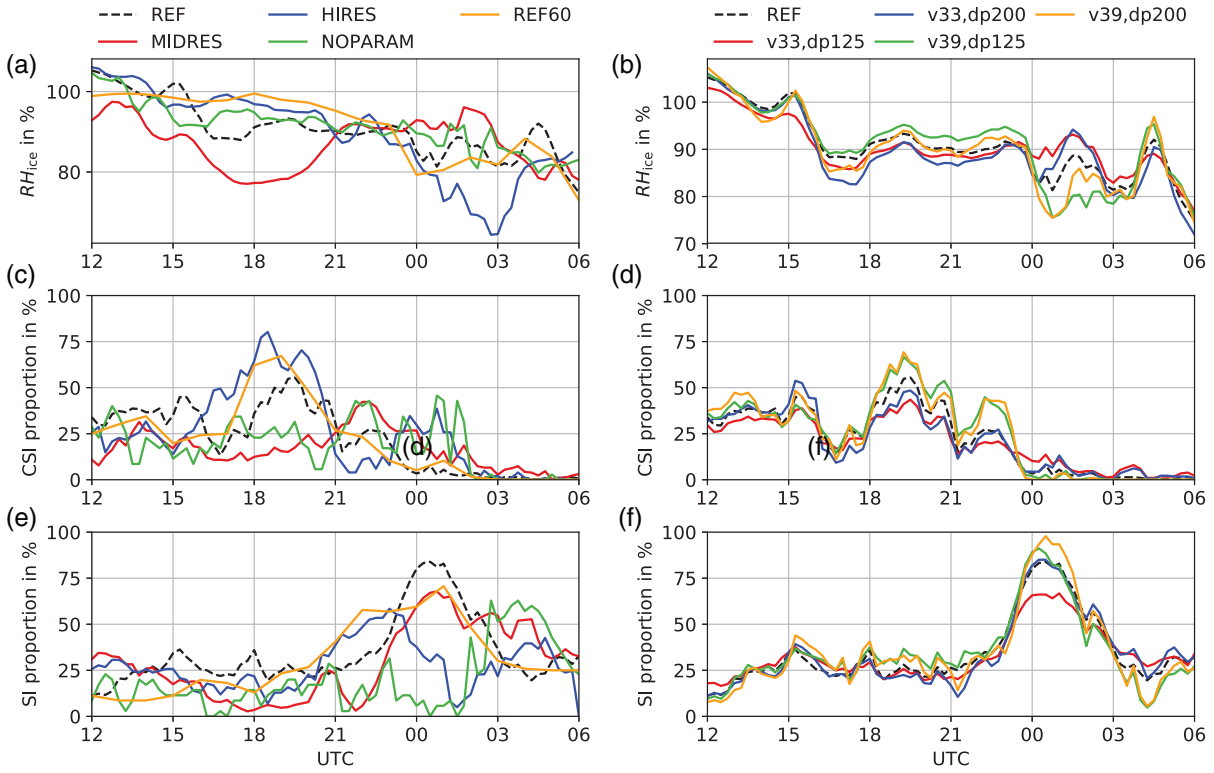

FIGURE 13 (a,b) Average values of relative humidity with respect to ice RH_{ice} , and fraction of trajectories satisfying (c,d) CSI and (e,f) SI criteria in sensitivity simulations to (a,c,d) horizontal resolution, model output frequency and convection parametrization, and (b,d,f) selection criteria. Trajectories are started at 13 January 2017, 0200 UTC and calculated backward to 12 January 2017, 1200 UTC and forward to 13 January 2017, 0600 UTC

both simulations maintain high humidity rather than the drying expected from other cases (Figure 13a). The Earth-relative wind speed also shows a similar acceleration in NOPARAM and REF (Figure 12d). In contrast, an increase in maximum system-relative wind speed by more than 5 $m \cdot s^{-1}$ can be seen in NOPARAM (Figure 12e). This shows that SJ trajectories are more accelerated when the convection parametrization is turned off. However, due to the more meridional path the resulting wind speed is partly compensated by travelling against the cyclone motion, which leads to a similar maximum in Earth-relative wind speed. It should also be kept in mind that the number of REF trajectories is almost nine times higher than in NOPARAM, hence contains a broader set of trajectories than just the most intense core. Finally, in both simulations θ_W values along SJ trajectories are nearly constant during the descent and differ by ~0.5 K only on average (Figure 12f) and evaporative cooling is again detected (Figure 12g,h).

In contrast with the consistency in evaporative cooling, the representation of convection strongly impacts on the contribution of CSI release (Figure 13c). The proportion of CSI trajectories in NOPARAM is close to values from MIDRES and fluctuates around 40% from 2130 UTC to around 0200 UTC, when the proportion decreases rapidly to 0%. Again, the difference is mainly caused by the proportion of II among trajectories, which is high in REF and low in NOPARAM around midnight (not shown). As defined in section 2.5 the presence of II excludes CSI. Figure 13e shows that the proportion of SI is below 25% most of the time and just begins to increase at around 0100 UTC when it is already decreasing in REF and reaches its maximum of circa 60% at around 0300 UTC. The proportion of trajectories satisfying stable conditions is higher in NOPARAM overall, although it should be kept in mind that only 35 trajectories are analysed.

4.2.3 | Temporal resolution of trajectory input data

The sensitivity of the trajectory computation to the model output frequency is tested by using hourly instead of quarter-hourly data from simulation REF (REF60; see section 2.3). This results in 116 trajectories satisfying the thresholds mentioned above, hence slightly less than REF. Differences between quarter-hourly and hourly model output frequency remain small in the path, pressure increase, maximum Earth-relative wind speed and evaporative cooling (Figure 12). Figure 13c,d further show a consistent proportion of CSI and SI. However, the dry-out around 1500 UTC discussed in section 4.1.2 cannot be identified in REF60, where RH_{ice} remains at almost 100% until 1800 UTC and slowly decreases from there (Figure 13a). The system-relative wind speed also increases ~3 h earlier but shows similar

behaviour from around 2200 UTC onward (Figure 12e). This is reminiscent of previous results by Volonté *et al.* (2018), who found a difference of 2 to 3 K in trajectories computed with hourly data. Nonetheless, the impact is much weaker in our case and thus does not appear to be significant here.

4.2.4 | Selection criteria

Stronger SJ trajectories, that is, trajectories which satisfy stronger wind speed and/or stronger descent criteria, might follow different dynamics than weaker ones. The robustness of results is tested here by varying thresholds used in the selection of SJ trajectories. For comparison, two thresholds are chosen for wind speed and pressure increase within 8 h, namely 33 and 39 $m \cdot s^{-1}$ and 125 and 200 hPa, respectively. The numbers of trajectories satisfying these conditions vary from 490 to 91, with increasing the pressure threshold only (227) having a lesser effect than increasing the wind threshold only (147).

Hardly any impact can be seen in the Earth-relative path, system-relative path and pressure increase (Figure S3a–c). However, a sensitivity to the threshold in wind speed is found in RH_{ice}. Trajectories exceeding 39 $m \cdot s^{-1}$ show a decrease around midnight by over 15% (Figure 13b). In contrast, trajectories exceeding 33 $m \cdot s^{-1}$ only slightly decrease at that time, before increasing again to over 90% at around 0200 UTC and eventually decreasing to ∼80% around 0300 UTC. Afterwards, the mean values of RH_{ice} remain similar. Unsurprisingly, increasing the threshold in wind speed also leads to a higher maximum of Earth-relative wind (Figure S3d). The impact is less straightforward in system-relative wind speed, where a first peak is slightly higher in trajectories with 33 $m \cdot s^{-1}$ thresholds, while a second peak exceeds the first one in trajectories with 39 $m \cdot s^{-1}$ threshold only (Figure S3d,e). Finally, the constant behaviour of θ_W is confirmed in all sets of trajectories, although those with the lower threshold in wind speed are on average 0.3 K cooler (Figure S3f), the reason for which is unclear. Similarly, the presence of evaporative cooling is suggested by all sets of trajectories but it is weaker for those with the lower pressure increase (Figure S3f,g,h).

The impact of thresholds on mesoscale instabilities is conspicuous. Figure 13d shows that trajectories fulfilling stronger constraints are related to enhanced CSI release. Both sets with wind speed required to exceed 39 $m \cdot s^{-1}$ show a maximum proportion of CSI trajectories of more than 60%. In contrast, the weaker wind speed threshold leads to values of less than 50%, although the trajectories with higher threshold in pressure increase show a slightly higher CSI proportion. This higher sensitivity to the threshold in wind speed is consistent with the contribution of CSI release to the SJ acceleration, hence stronger winds are reached with a higher proportion of CSI trajectories. This conclusion is further supported by the fact that all sets of trajectories show an almost equal pressure increase. Overall, changing the threshold in wind speed impacts results for SJ trajectories more than changing the threshold in pressure increase. This is not so clear for SI (Figure 13f). Only trajectories with both low criteria for wind speed and pressure show a smaller proportion of SI during the maximum shortly after midnight. Consistently trajectories with both high criteria for wind speed and pressure show a higher proportion of trajectories satisfying mesoscale instability criteria.

5 | ROLE OF OROGRAPHY AND SURFACE PROPERTIES

To the best of our knowledge, no SJ case over continental Europe has ever been analysed in the scientific literature. The case of *Egon* thus provides a unique chance to investigate the role of topography in the evolution of an SJ by analysing the three additional simulations FLAT, SEA and SST (see section 2.2) in comparison to REF.

5.1 | Synoptic evolution

Figure 14 shows minimum core pressure and storm track analogous to Figure 4. Until 1900 UTC on 12 January 2017, time of arrival of the cyclone at the French coast, all simulations show an almost identical evolution of core pressure (Figure 14a). However, the four simulations strongly diverge from that time onwards, and each change in surface properties from REF to FLAT, SEA and SST leads to a more intense evolution. The sensitivity to the model resolution has additionally been tested and systematically resulted in slightly lower core pressure with coarser resolution, but confirmed the divergence between the four configurations (not shown). The track is also impacted and is shifted 100 km further south over Germany in all simulations without orography (Figure 14b). This southern shift appears to be mainly due to the removal of the Alps, the principal mountain range in the region.

While the minimum pressure during the evolution in REF is 978 hPa, FLAT reaches 972 hPa about 8 h later (Figure 14a). This shows that orography plays a crucial role in deepening the cyclone. The impact is partly due to the contribution of resolved and subgrid-scale orography to the surface roughness, since mountains cause more friction than lowlands. Furthermore, the Alps block warm and moist air from the Mediterranean Sea in REF and prevent it from travelling northwards as in FLAT (Figure 15a,b). On the other hand, the Alps appear to cause a föhn effect on their northern side (Figure 3b,c), which may have supported cyclone deepening in REF.

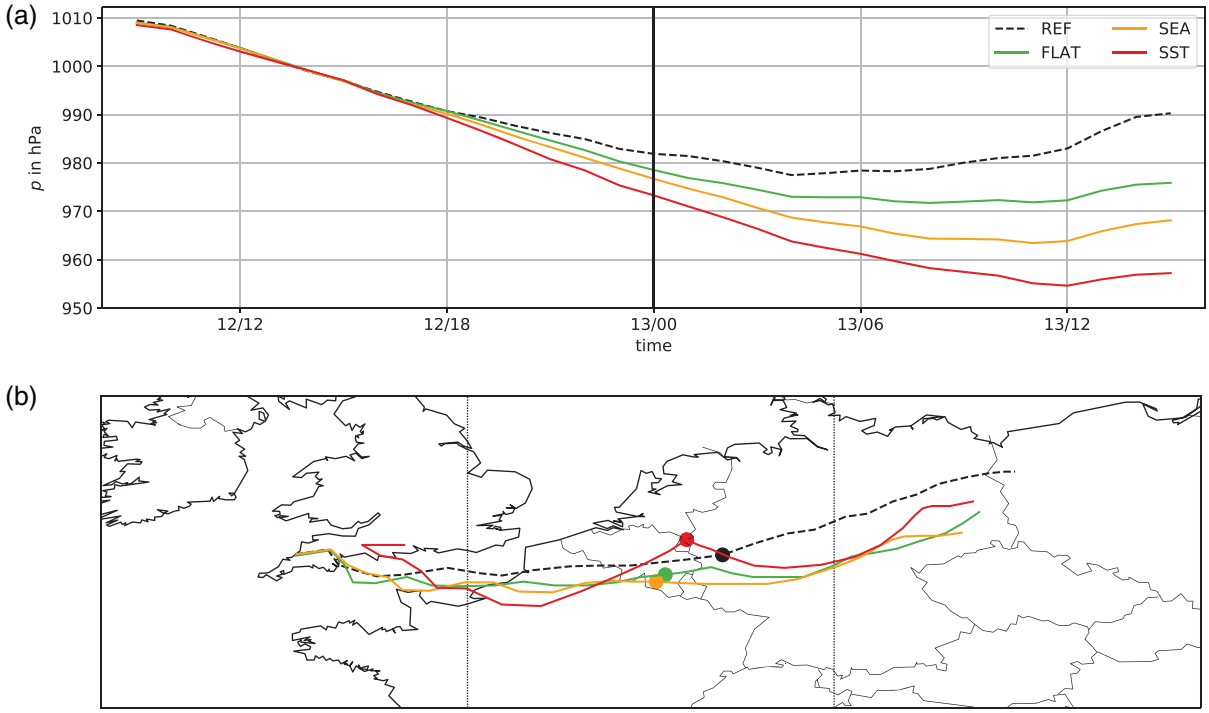

FIGURE 14 Comparison of REF with simulations without orography but surface roughness of land (FLAT), surface roughness of sea but SSTs of land (SEA) and surface roughness and SSTs of sea (SST) from 12 January 2017, 0900 UTC to 13 January 2017, 1400 UTC through (a) core pressure and (b) storm track. The solid black line in (a) and markers in (b) mark the time shown in Figure 15, that is, 0000 UTC on 13 January

Core pressure in the SEA simulation even reaches a minimum of 964 hPa about 11 h later than the REF minimum (Figure 14a). Changes in friction appear to be the most important factor here: since the surface roughness of ocean is much lower than that of land, the cyclone experiences less filling through Ekman effects. Furthermore, the ocean is a humidity source, which may help the cyclone deepen even further in SEA. However, differences in equivalent potential temperature θ_E at 850 hPa between FLAT and SEA (Figure 15b,c) are not large, suggesting that the time is likely too short for this to be a major effect. Finally, the core pressure of the SST simulation goes down to ~955 hPa around noon on 13 January. The difference between the SEA and SST simulations shows that the warmer surface temperatures enhance turbulent fluxes and provide another essential source of energy during cyclogenesis (Figure 15d).

5.2 | Sting jet

Earth- and system-relative wind speed at 850 hPa analogous to Figure 6 are shown for FLAT, SEA and SST in Figure 16. For each simulation, a time of strong winds within the frontal-fracture region is chosen when the bent-back front is not yet fully wrapped around the cyclone centre. This helps identifying the sometimes difficult separation between SJ and CJ. For FLAT the chosen time is 0000 UTC on 13 January 2017, for SEA 0100 UTC and for SST 0200 UTC.

Winds located east of the cold front, hence caused by the WJ, are ~5 $m \cdot s^{-1}$ weaker at 850 hPa in all simulations without orography. This may be related to blocking and channelling effects by the Alps and other orographic barriers. High wind speeds located near the frontal-fracture zone, hence related to the SJ, appear in Earth-relative wind speed at around 2000 UTC in all four simulations with similar strength (not shown). In the SST simulation first indications are already seen in the system-relative wind speed around 1800 UTC. In FLAT and SEA wind speeds related to the SJ increase fast, reach their maximum ~1 h earlier than REF and begin to weaken at around 0200 UTC (Figure 16a,c). At that time the system-relative wind speed is rather low in FLAT and SEA (Figure 16b,d). Considering all times, however, the CJ is weaker but more widespread in FLAT than in REF, but stronger in SEA (not shown), pointing to a rather complicated response mechanism.

In comparison, the SST simulation shows a weaker SJ first but with a rapid strengthening at around 0200 UTC (Figure 16e). At the same time, the system-relative wind speed in Figure 16f decreases shortly, before increasing again, indicating the formation of the CJ. The Earth-relative wind speed reaches very high values throughout a longer time than in the other simulations, beginning to slowly weaken shortly before noon on 13 January (not shown). A smooth transition between system- and Earth-relative wind speeds in these later stages makes a clear separation between SJ and CJ difficult.

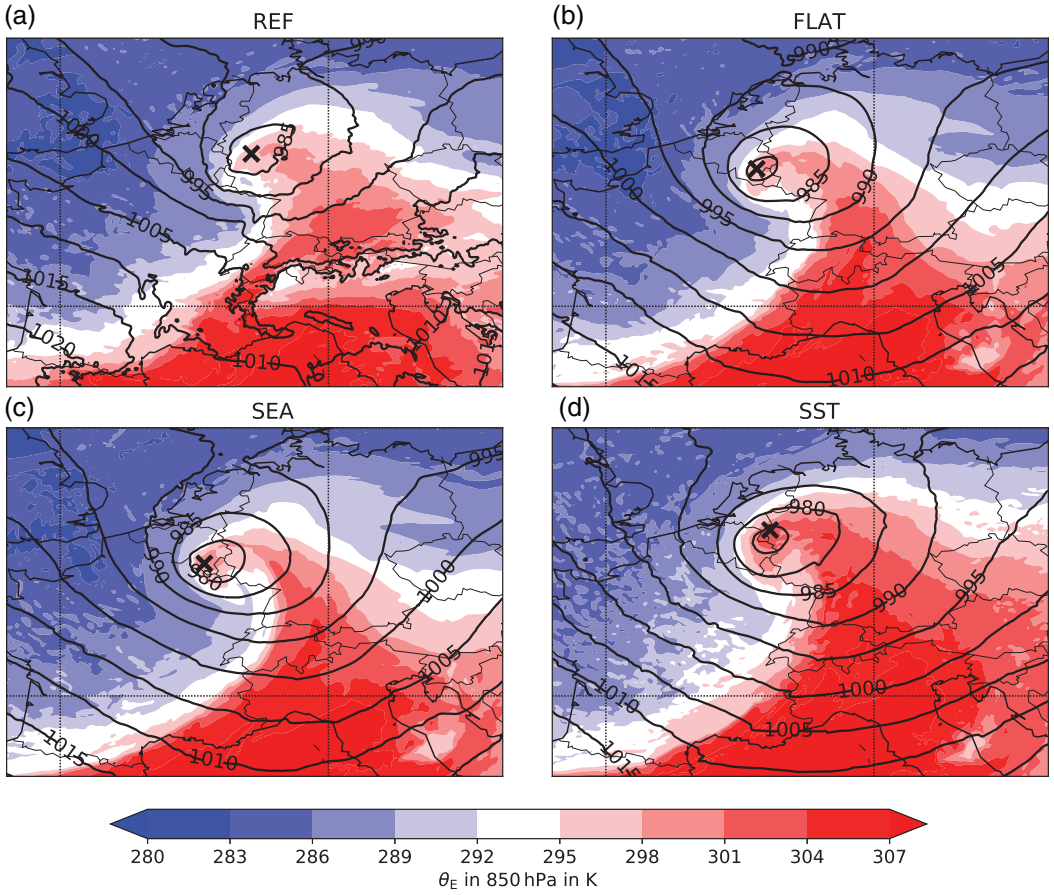

FIGURE 15 Equivalent potential temperature θ_E at 850 hPa and surface pressure in simulations (a) REF, (b) FLAT, (c) SEA and (d) SST on 13 January 2017, 0000 UTC. The cyclone centre is marked by the black crosses

For the computation of SJ trajectories, the starting times are those as shown in Figure 16, hence 13 January, 0000 UTC for FLAT, 0100 UTC for SEA and 0200 UTC for SST. Although the SJ might be causing stronger winds later in SST, an early time is chosen for a clearer separation from the CJ. The wind speed threshold is changed to 36 $m \cdot s^{-1}$ for FLAT, 38 $m \cdot s^{-1}$ for SEA and 42 $m \cdot s^{-1}$ for SST, because the strength of the winds differs so much between these simulations (section 5.2). The pressure increase threshold of 150 hPa used in section 4.1, however, remains unchanged. These criteria lead to 177 trajectories for FLAT, 207 trajectories for SEA and 152 trajectories for SST. Figure 17 shows various parameters along trajectories analogous to Figure 9. For better comparison between the simulations, averaged values and a time-scale relative to the starting time of trajectories are chosen.

The Earth-relative paths of SJ trajectories in FLAT and SEA are similar to REF, but with a slightly more meridional component in the beginning ~200 km north of REF (Figure 17a). Over France the trajectories cross those in REF and remain ~100 km south until the end of the calculation. The FLAT and SEA trajectories remain at a stable distance of ~50 km from each other. The trajectory path in SST starts almost 250 km north of REF over northern England, remains zonal and turns south where the northern Netherlands would be. Again, the system-relative path looks similar in FLAT and SEA (Figure 17b). SST shows a more circular track than in REF, FLAT and SEA. In the cases of REF, FLAT and SEA the descent starts ~10 h before the reference time, but in FLAT and SEA it originates from almost 100 hPa higher pressure than in REF (Figure 17c). While REF trajectories stay close to 600 hPa at first, SST trajectories already descend with a rate similar to REF's later descent rate. Around reference time SST trajectories show a drop of almost 100 hPa in less than an hour.

All simulations show similar behaviour of RH_{ice} from around −5 to 5 h. In contrast to REF, FLAT and SEA trajectories, a dry phase can be seen in SST trajectories until ~7 h before reference time (Figure 17d). As this decrease to almost 50% happens while the trajectories are still at mid-levels, it does not match the dry-out observed for other cases. Furthermore, the decrease suggests that the SJ trajectories are not within the cloud head at this early stage. Reaching almost 700 hPa, RH_{ice} increases to nearly saturated conditions before showing another drop of more than ~30% starting shortly before the reference time. FLAT and SEA also show a weak decrease an hour earlier.

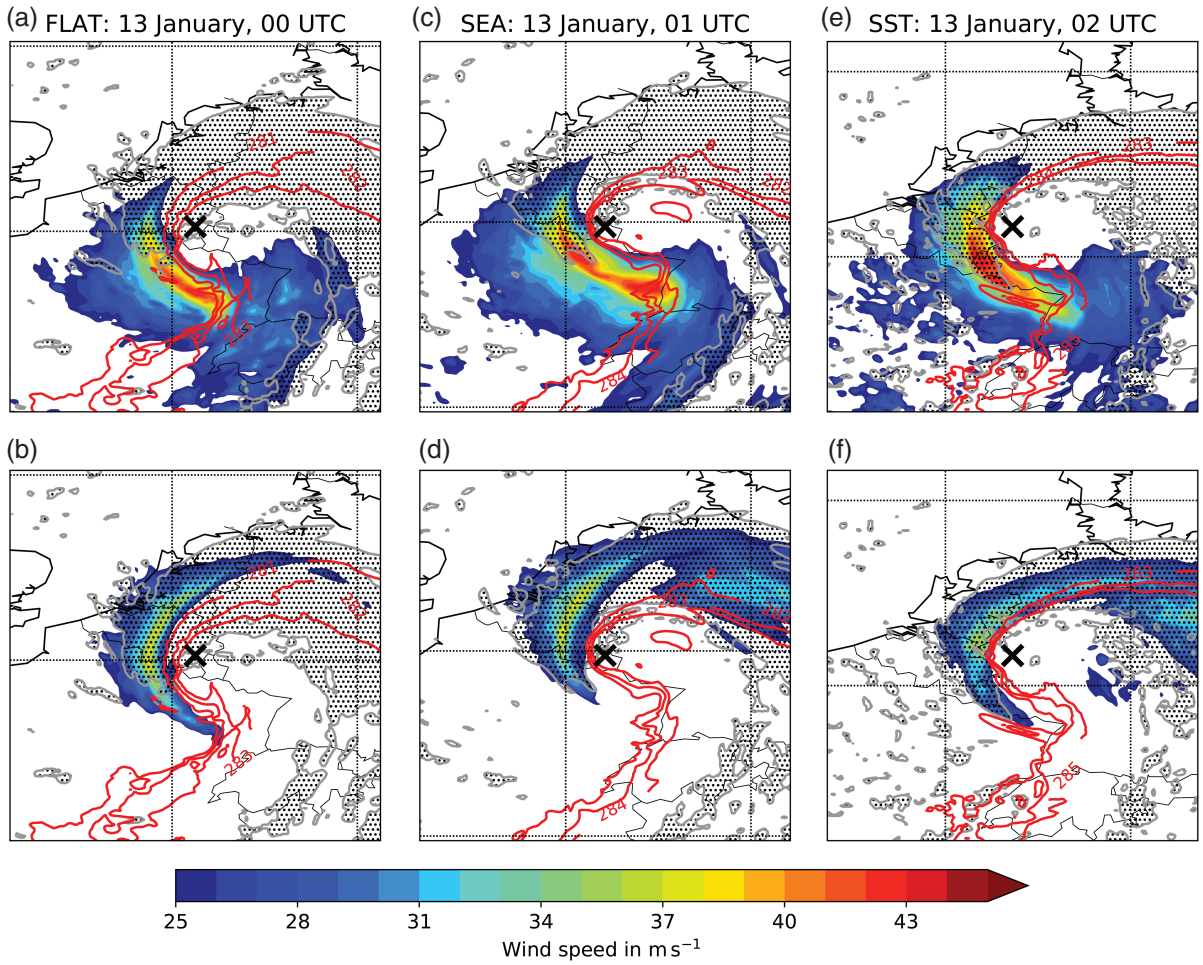

FIGURE 16 (a,c,e) Earth-relative and (b,d,f) system-relative wind speed at 850 hPa (shading), cloud cover >80% (dotted area), three equivalent potential temperature contours at 850 hPa representing the frontal zone (red contours) and cyclone centre (cross) of simulations (a,b) FLAT, (c,d) SEA and (e,f) SST for a chosen time representing the strength of the sting jet

The maximum of Earth-relative wind speed in SST is just slightly higher than in the other simulations (Figure 17e). In comparison, SST trajectories started at 0600 UTC show maximum Earth-relative wind speeds around 10 m·s^{-1} higher than REF and suggest a stronger SJ. The acceleration starts ∼5 h before the reference time, when SST trajectories also start to accelerate in system-relative wind speed (Figure 17f). REF, FLAT and SEA already accelerate slowly ∼10 h before reference time. In contrast to Earth-relative wind speed where the maxima of FLAT and SEA are slightly weaker than REF, the system-relative wind speed is ∼6 m·s^{-1} stronger in FLAT and similar in SEA. This indicates that the faster cyclone movement in REF (Figure 14b) contributes to the Earth-relative wind speed. The development of both Earth- and system-relative wind speed of FLAT and SEA is almost identical. This suggests that the orography has more influence than the surface roughness considering the same surface temperatures.

Similar to REF, simulations without orography show nearly constant values of θ_W during the descent (Figure 17g). Reaching the boundary layer, REF trajectories show a weak warming around reference time. As the boundary layer is lower in FLAT and SEA due to no orography and no additional heat fluxes, the trajectories show no increase at all. Furthermore, all simulations show a decrease in θ during the descent combined with an increase in q (Figure 17h,i), which again is a sign of contribution of evaporative cooling. However, θ_W of SST trajectories, which is about ∼1 K lower, begins increasing notably around 5 h before reference time. At around −3 h up to the reference time the values show again stable behaviour before increasing rapidly. This is consistent with stable values of θ and q at the same time before decreasing and increasing rapidly, respectively. The strong decrease and increase in θ and q, respectively, is in turn consistent with the pressure drop mentioned above. Additionally, θ shows an increase by almost 5 K starting shortly after reference time in SST trajectories. The warming of θ_W and θ suggests that surface heat fluxes and vertical mixing influence the trajectories at these times.

Figure 17j shows the proportion of trajectories satisfying the CSI criteria defined in section 2. As discussed in section 4, REF trajectories show a decrease by more than 60% to almost

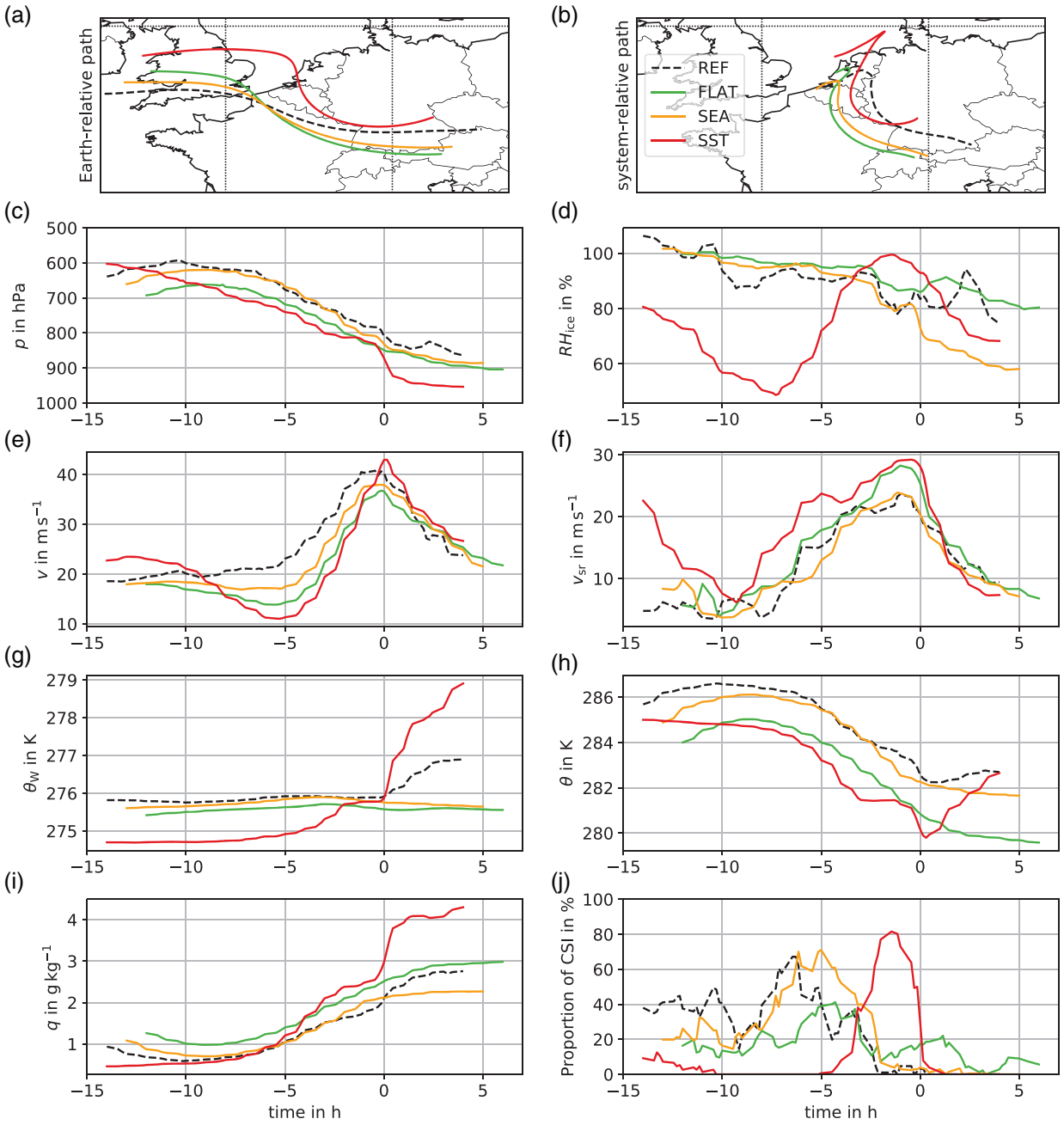

FIGURE 17 Average values along trajectories for (a) Earth-relative path, (b) system-relative path, (c) pressure, (d) relative humidity with respect to ice, (e) wind speed, (f) system-relative wind speed, (g) wet-bulb potential temperature, (h) potential temperature and (i) specific humidity. (j) The fraction of trajectories satisfying CSI criteria. Trajectories are started at 13 January 2017, 0000 UTC (FLAT), 0100 UTC (SEA), 0200 UTC (REF) and 0200 UTC (SST) and calculated backwards to 1200 UTC and forwards to 0600 UTC. Wind speed must exceed 36, 38 and 42 $m \cdot s^{-1}$ (FLAT, SEA, SST, respectively) at starting time and pressure must decrease by 150 hPa in 8 h. The time is relative to the starting time of trajectories

zero during the descent, thus indicating CSI release. A similar behaviour can be seen in the SEA simulation, where the CSI proportion decreases by over 70% an hour later than REF. FLAT trajectories also show a decrease but not as strong, only reaching a maximum of ~40%. Consistent with this is the decrease in the vertical component of absolute vorticity ζ_z to negative values, indicating II around 2 to 3 h before reference time (not shown), as well as the increase in *MPV* *. The proportion of CSI in the SST simulation only starts increasing about 5 h before reference time, when it already decreases in the other simulations. This delay is associated with the late increase in RH_{ice} (Figure 17d). Around 0 h also the CSI proportion in SST decreases from ~80% to zero mainly due to increasing of CI. Note that FLAT shows lower CSI proportion than the other simulations but higher system-relative wind speeds than REF and SEA

(Figure 17f). A linkage between CSI and high winds is not as straightforward in FLAT and illustrates the multiple factors that determine the ultimate strength of an SJ.

5.3 | Surface gust speeds

After confirming the presence of an SJ in all simulations without orography, it is of interest to investigate the effect on the surface. It is expected that wind and gust speeds with modified topography in SEA and SST exceed those with the surface roughness of land. Moreover, the comparison between REF and FLAT allows investigating how the orography influences the wind.

Figure 18 shows the footprint of maximum simulated gust speeds at 10 m from 12 January, 0000 UTC to 14 January, 0000 UTC. Gust speeds over northern France, which are associated with the SJ, occur with similar strength in FLAT compared to REF (Figures 5a and 18a). In contrast, the exceptional high gusts near the French-German border do not stand out in FLAT. The more southern storm track without orography in FLAT leads to the footprint missing the Ore Mountains, where high gusts were measured (Figure 1a) and simulated in REF (Figure 5b). Instead, the footprint in FLAT reaches the region of the Bavarian and Bohemian forests near the German-Czech border but without strong gusts in the absence of the orography (Figure 18a). Nonetheless, a clear gust footprint comparable to that with orography covers northern France and southern Germany.

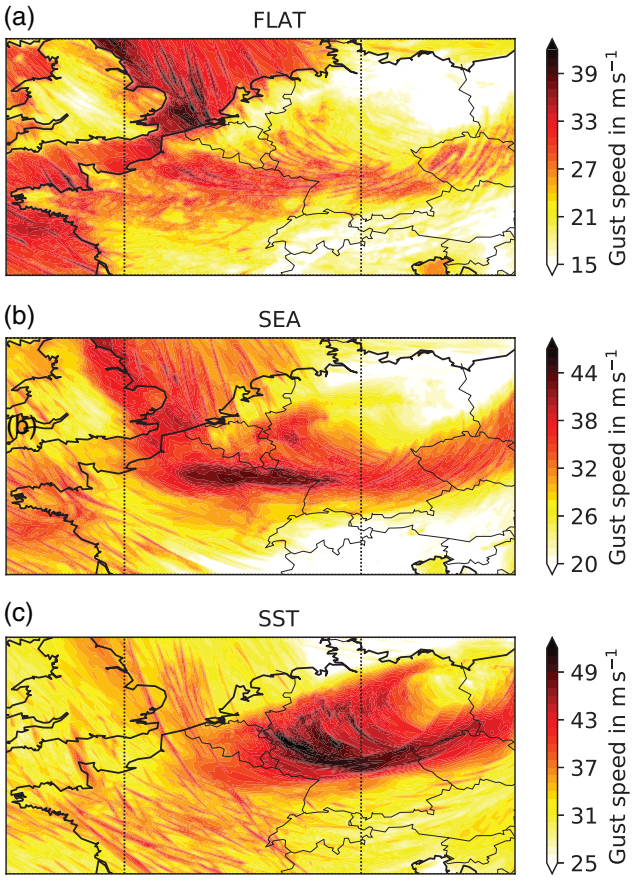

FIGURE 18 Footprint of simulated maximum 10 m gust speeds from 12 January 2017, 0000 UTC to 14 January 2017, 0000 UTC for simulations without orography (a) FLAT, (b) SEA and (c) SST. Note that the scale of FLAT is the same as for REF in Figure 5, while it is adjusted to the strength of SEA and SST

Gusts in SEA are much stronger, mainly because the storm itself is more intense but also because less deceleration of winds occurs due to the reduced friction (Figure 18b). Gusts over northern France are even stronger than over Germany. As in FLAT, the footprint over Germany and farther east is shifted south due to the shifted storm track. A further enhancement can be seen with the even deeper cyclogenesis with higher surface temperatures in the SST simulation (Figure 18c). In this case, the highest gusts occur later and over Germany due to the different track and longer lasting intensification (Figure 14a). Wind speeds at higher levels are expected to be less disturbed by the change of orography and surface roughness than those near the surface. However, the warmer sea also increases turbulent transport of momentum, which should tend to increase surface gusts and decrease 850 hPa wind speeds. Disentangling the individual contribution of all of these factors is challenging. Overall, however, we can state that changing the surface roughness and sea-surface temperatures influences the strength and extent of gusts much more than flattening the orography.

6 | CONCLUSIONS

An SJ is an air stream near the tip of the bent-back front of a rapidly intensifying Shapiro–Keyser cyclone. SJs descend from mid-levels within the cloud head into the frontal-fracture region, where they can cause strong surface winds. Due to their small scale and short lifetime, predicting SJs remains a challenge. Here we presented a detailed analysis of the dynamics of SJ-storm *Egon* (12–13 January 2017), which caused surface wind gusts of almost 150 km·h^{-1} over northern France and south-central Germany. With SJ occurring most frequently over the North Atlantic and the British Isles, such a long SJ trajectory over land had not yet been documented and allowed investigating the impact of orography, roughness and surface fluxes on SJ dynamics for the first time. The roles of mesoscale instabilities (e.g. CSI and SI) and evaporative cooling for *Egon*'s SJ were examined in detail based on trajectories. In addition to surface wind observations, the investigation was based on a series of simulations using the ICON model in limited-area mode with the ICON-EU forecasts as boundary conditions. Runs with and without convective parametrization and with different horizontal grid spacings (6.5, 3.3 and 1.6 km) and numbers of vertical levels (50 and 90) revealed the sensitivity to model configuration. The main conclusions are given in the following and are also summarised qualitatively in Table 2.

TABLE 2 Summary of simulation results for intensity, gusts, wind and SJ trajectories. Trajectories are selected with a wind speed threshold of 35 m·s^{-1} and a pressure increase by at least 125 hPa in 8 h. Values of Δp, v_{max} and $v_{sr,\,max}$ are averaged over all selected trajectories. The symbols ∼, − and + indicate qualitatively the degree of deviation from the REF simulation. Note that in the first line positive is defined in terms of intensity such that a plus implies a deeper pressure

	REF	MIDRES	HIRES	NOPARAM	REF60	FLAT	SEA	SST
Intensity (core pressure minimum)	977.5 hPa	∼	−	−		+	++	+++
98th percentile of gust speed	32.6 m·s^{-1}	+	∼	∼		∼	++	+++
98th percentile of 850 hPa wind speed	38.8 m·s^{-1}	+	+	∼		∼	+	++
Fraction of gusts >30 m·s^{-1}	5.26%	+	+	∼		∼	++	+++
Number of SJ trajectories	292	∼	− −	− − −	− −	∼	∼	+++
Pressure increase Δp	281 hPa	∼	− −	− −	− −	−	∼	++
Peak Earth-relative wind v_{max}	39.5 m·s^{-1}	−	−	− −	∼	−	∼	+
Peak system-relative wind $v_{sr,\,max}$	23.1 m·s^{-1}	∼	−	++	∼	+	∼	++
Maximum proportion of CSI	55.5%	−	++	−	+	−	∼	∼

ICON simulations reproduce the storm evolution sufficiently but delay the explosive deepening, shift the track southward over Belgium and Germany, and underestimate wind gusts over land. Storm characteristics show a weak sensitivity to varying grid spacing between 1.6 and 6.5 km. Switching off the convection parametrization at 3.3 km grid spacing improves correlations with surface observations but deteriorates the mean error, while the run with 1.6 km shows the overall best performance. Remarkably, the SJ and the associated surface gust footprint are weaker in simulations without convection parametrization at 3.3 km grid spacing, further enhancing the general underestimation in ICON. It is plausible that isolated small-scale convection, for example, behind the cold front, is still not sufficiently represented at this resolution. However, only weak differences were found in convective precipitation amounts. The dynamical analysis was then mostly based on the simulation with 3.3 km grid spacing, 90 vertical levels and convection parametrization switched on.

High wind speeds at 850 hPa within the frontal-fracture region suggest that the SJ occurred between 2200 UTC and 0500 UTC. Trajectories calculated from the 3D wind fields using LAGRANTO with a time step of 15 min confirm this. Trajectories started at 0200 UTC reveal a descending airstream from over 600 hPa down to the boundary layer, a marked acceleration of more than 18 m·s^{-1} in both Earth- and system-relative wind speed and constant values of wet-bulb potential temperature θ_W, consistent with previous case-studies (Baker *et al.*, 2014). Interestingly, the decrease in RH_{ice} during descent found in many other cases is weak here with values mostly remaining above 80% and cloud cover reaching down to 900 hPa. Changes in specific moisture and potential temperature suggest that this behaviour is mostly caused by evaporative cooling. Consistent with previous cases, the descent and acceleration of SJ trajectories appear to be related to CSI in early stages followed by similar contributions from SI and II. Finally, vertical mixing facilitated by CI may help transport momentum into the boundary layer.

Trajectories were also computed for 6.5 and 1.6 km horizontal grid spacing, hourly (instead of 15 min) data input and 3.3 km horizontal grid spacing without convection parametrization (see Table 2). Furthermore, differing wind and pressure difference criteria for the selection of SJ trajectories were tested. Between these, there is a good consistency with respect to SJ characteristics such as descent from mid-levels on surfaces of constant θ_W, acceleration, moderate drying and indications of evaporative cooling, but the number of identified SJ trajectories and the level and type of mesoscale instabilities vary markedly. The stronger the winds and/or the deeper the descent, the greater the contribution of CSI, SI and II, which emphasises collectively the importance of mesoscale instabilities.

To examine the influence of orography, land surface characteristics and surface temperatures, three further simulations were computed (see Table 2). The first one with flattened orography (FLAT), the second with surface roughness and other surface parameters changed to water (SEA), and the last with an additional extrapolation of the warmer temperatures over adjacent oceans to the land areas (SST). Each of the changes described above led to a delay in the filling of the cyclone and thus a deeper core pressure. Removing the Alps allowed warm and moist air from the Mediterranean to move northwards, where it helps deepen the cyclone and shift the storm track southward by ∼100 km. Wrapping up more quickly, the system velocity is slower than in the reference simulation (REF). All three sensitivity simulations show a clear SJ. While slightly weaker than the REF simulation in FLAT and SEA, the SJ is stronger in the SST simulation. Most variables along SJ trajectories show consistent behaviour including high RH_{ice} in the FLAT and SEA

simulations. However, the SJ is rather dry in the beginning and then gets moister ahead of the SJ development in SST simulations, where the track deviates most strongly from the other cases. CSI is present in all simulations but with large deviations. FLAT shows suppressed release, while the SST simulation is too dry for CSI for much of the early stages but shows a peak when already descended to below 800 hPa. As the SJ in FLAT and SEA evolves similarly, the warmer surface temperatures in SST are suggested to be the main cause of a stronger SJ by intensifying the deepening of the cyclone as a whole. The results also show that roughness is a major control on surface wind gusts for comparable storm intensities.

Overall, this study has demonstrated how the combined effects of warm air blocking by the Alps, higher roughness and reduced surface fluxes cause an SJ cyclone to fill more quickly and to move on a faster, more northern track across central Europe, while results are not particularly sensitive to the details of the model configuration and employed thresholds tested here. The SJ response to the different aspects of the land passage is complex, showing some compensating effects. This work has demonstrated for the first time that SJs can occur in continental Europe and that weather forecasters should be more aware of the associated risks related to potential mis-forecasts. To confirm this, similar analyses should be applied to other recent reports of suspected SJs in western and central Europe, carefully evaluating the quality of forecasts for different lead times. This is a pressing concern, as the potential of SJ storms may increase in this region with climate change (see Fig. 3 in Martínez-Alvarado *et al.* (2018)). Another potentially interesting aspect is the relatively large contribution from evaporative cooling in this case. We suspect that this aspect is mostly related to the individual dynamics of storm *Egon* but a deeper insight into the control mechanisms on evaporative cooling contributions to SJ is still lacking.

ACKNOWLEDGEMENTS

The authors thank Gregor Pante for his help at running ICON-LAM simulations and Joaquim G. Pinto for helpful comments on the design of the study. SYNOP observations were gathered from ogimet.com, while observations from the DWD surface network were downloaded from the Climate Data Center at ftp://ftp-cdc.dwd.de/pub/CDC/. The VIIRS image in Figure 1b was taken from NERC Satellite Receiving Station, Dundee University, Scotland at http://www.sat.dundee.ac.uk (site now closed). The research leading to these results has been done within the project C5 "Forecast uncertainty for peak surface gusts associated with European cold-season cyclones" of the Transregional Collaborative Research Center SFB/TRR 165 "Waves to Weather," funded by the German Research Foundation (DFG). The authors also acknowledge the two reviewers, Gwendal Rivière and Ambrogio Volonté, for their critical comments, which helped to improve this article.

ORCID

Lea Eisenstein https://orcid.org/0000-0001-9977-0176
Florian Pantillon https://orcid.org/0000-0001-7205-4428
Peter Knippertz https://orcid.org/0000-0001-9856-619X

REFERENCES

Baker, L. (2009) Sting jets in severe northern European wind storms. *Weather*, 64(6), 143–148.

Baker, L.H., Gray, S.L. and Clark, P.A. (2014) Idealised simulations of sting-jet cyclones. *Quarterly Journal of the Royal Meteorological Society*, 140, 96–110.

Bechtold, P., Köhler, M., Jung, T., Doblas-Reyes, F., Leutbecher, M., Rodwell, M.J., Vitart, F. and Balsamo, G. (2008) Advances in simulating atmospheric variability with the ECMWF model: from synoptic to decadal time-scales. *Quarterly Journal of the Royal Meteorological Society*, 134, 1337–1351.

Brâncuş, M., Schultz, D.M., Antonescu, B., Dearden, C. and Ştefan, S. (2019) Origin of strong winds in an explosive Mediterranean extratropical cyclone. *Monthly Weather Review, 147(10), 3649–3671*.

Browning, K.A. (2004) The sting at the end of the tail: damaging winds associated with extratropical cyclones. *Quarterly Journal of the Royal Meteorological Society*, 130, 375–399.

Browning, K.A., Smart, D.J., Clark, M.R. and Illingworth, A.J. (2015) The role of evaporating showers in the transfer of sting-jet momentum to the surface. *Quarterly Journal of the Royal Meteorological Society*, 141, 2956–2971.

Catto, J.L. (2016) Extratropical cyclone classification and its use in climate studies. *Reviews of Geophysics*, 54, 486–520.

Clark, P.A., Browning, K.A. and Wang, C. (2005) The sting at the end of the tail: model diagnostics of fine-scale three-dimensional structure of the cloud head. *Quarterly Journal of the Royal Meteorological Society*, 131, 2263–2292.

Clark, P.A. and Gray, S.L. (2018) Sting jets in extratropical cyclones: a review. *Quarterly Journal of the Royal Meteorological Society*, 144(713), 943–969.

Coronel, B., Ricard, D., Rivière, G. and Arbogast, P. (2016) Cold-conveyor-belt jet, sting jet and slantwise circulations in idealized simulations of extratropical cyclones. *Quarterly Journal of the Royal Meteorological Society*, 142, 1781–1796.

Doms, G., Förstner, J., Heise, E., Herzog, H.-J., Mironov, D., Raschendorfer, M., Reinhardt, T., Ritter, B., Schrodin, R., Schulz, J.-P. and Vogel, G. (2011) *A description of the nonhydrostatic regional COSMO model: Part II: physical parameterization*. Consortium for Small-Scale Modelling. Available at: http://cosmo-model.org [Accessed 8th November 2019].

Earl, N., Dorling, S., Starks, M. and Finch, R. (2017) Subsynoptic-scale features associated with extreme surface gusts in UK extratropical cyclone events. *Geophysical Research Letters*, 44, 3932–3940.

Fink, A.H., Brücher, T., Ermert, V., Krüger, A. and Pinto, J.G. (2009) The European storm *Kyrill* in January 2007: synoptic evolution, meteorological impacts and some considerations with respect to climate change. *Natural Hazards and Earth System Sciences*, 9, 405–423.

Gray, S.L., Martínez-Alvarado, O., Baker, L.H. and Clark, P.A. (2011) Conditional symmetric instability in sting-jet storms. *Quarterly Journal of the Royal Meteorological Society*, 137, 1482–1500.

Hart, N.C.G., Gray, S.L. and Clark, P.A. (2017) Sting-jet windstorms over the North Atlantic: climatology and contribution to extreme wind risk. *Journal of Climate*, 30, 5455–5471.

Hewson, T.D. and Neu, U. (2015) Cyclones, windstorms and the IMILAST project. *Tellus A*, 67, 27128.

Knippertz, P., Pantillon, F. and Fink, A.H. (2018) The devil in the detail of storms. *Environmental Research Letters*, 13, 051001.

Leuenberger, D., Koller, M., Fuhrer, O. and Schär, C. (2010) A generalization of the SLEVE vertical coordinate. *Monthly Weather Review*, 138, 3683–3689.

Martínez-Alvarado, O., Baker, L.H., Gray, S.L., Methven, J. and Plant, R.S. (2014) Distinguishing the cold conveyor belt and sting jet airstreams in an intense extratropical cyclone. *Monthly Weather Review*, 142, 2571–2595.

Martínez-Alvarado, O., Gray, S.L., Catto, J.L. and Clark, P.A. (2012) Sting jets in intense winter North-Atlantic windstorms. *Environmental Research Letters*, 9, 039501.

Martínez-Alvarado, O., Gray, S.L., Hart, N.C.G., Clark, P.A., Hodges, K.I. and Roberts, M.J. (2018) Increased wind risk from sting-jet windstorms with climate change. *Environmental Research Letters*, 13, 044002.

Mlawer, E.J., Taubman, S.J., Brown, P.D., Iacono, M.J. and Clough, S.A. (1997) Radiative transfer for inhomogeneous atmospheres: RRTM, a validated correlated-k model for the longwave. *Journal of Geophysical Research*, 102(D14), 16663–16682.

Pantillon, F., Lerch, S., Knippertz, P. and Corsmeier, U. (2018) Forecasting wind gusts in winter storms using a calibrated convection-permitting ensemble. *Quarterly Journal of the Royal Meteorological Society*, 144(715), 1864–1881.

Parker, D.J. (1998) Secondary frontal waves in the North Atlantic region: a dynamical perspective of current ideas. *Quarterly Journal of the Royal Meteorological Society*, 124, 829–856.

Parton, G.A., Vaughan, G., Norton, E.G., Browning, K.A. and Clark, P.A. (2009) Wind profiler observations of a sting jet. *Quarterly Journal of the Royal Meteorological Society*, 135, 663–680.

PERILS AG (2018) *PERILS discloses fourth and final loss estimate for extratropical cyclone Egon of EUR 275m*. Available at: https://www.perils.org/losses [Accessed 20th November 2018].

Raschendorfer, M. (2001) *The new turbulence parameterization of LM*. Consortium for Small-Scale Modelling. *COSMO Newsletter*, 1, 89–97.

Rautenhaus, M., Kern, M., Schäfler, A. and Westermann, R. (2015) Three-dimensional visualization of ensemble weather forecasts. Part 1: The visualization tool Met.3D (version 1.0). *Geoscientific Model Development*, 8, 2329–2353.

Sanders, F. and Gyakum, J.R. (1980) Synoptic-dynamic climatology of the "bomb". *Monthly Weather Review*, 108, 1589–1606.

Schmoeckel, J. and Kottmeier, C. (2008) Storm damage in the Black Forest caused by the winter storm "*Lothar*". Part 1: Airborne damage assessment. *Natural Hazards and Earth System Sciences*, 8, 795–803.

Schneider, L., Barthlott, C., Barrett, A.I. and Hoose, C. (2018) The precipitation response to variable terrain forcing over low mountain ranges in different weather regimes. *Quarterly Journal of the Royal Meteorological Society*, 144(713), 970–989.

Schultz, D.M. and Browning, K.A. (2017) What is a sting jet? *Weather*, 72(3), 63–66.

Schultz, D.M. and Sienkiewicz, J.M. (2013) Using frontogenesis to identify sting jets in extratropical cyclones. *Weather and Forecasting*, 28, 603–613.

Schultz, J.P. (2008) Revision of the turbulent gust diagnostics in the COSMO model. *COSMO Newsletter*, 8, 17–22. Available at: http://www2.cosmo-model.org/content/model/documentation/newsLetters/newsLetter08/cnl8_schulz.pdf [Accessed 21st March 2019].

Slater, T.P., Schultz, D.M. and Vaughan, G. (2015) Acceleration of near-surface strong winds in a dry, idealised extratropical cyclone. *Quarterly Journal of the Royal Meteorological Society*, 141, 1004–1016.

Slater, T.P., Schultz, D.M. and Vaughan, G. (2017) Near-surface strong winds in a marine extratropical cyclone: acceleration of the winds and the importance of surface fluxes. *Quarterly Journal of the Royal Meteorological Society*, 143(702), 321–332.

Smart, D.J. and Browning, K.A. (2014) Attribution of strong winds to a cold conveyor belt and sting jet. *Quarterly Journal of the Royal Meteorological Society*, 140, 595–610.

Sprenger, M. and Wernli, H. (2015) The LAGRANTO Lagrangian analysis tool – version 2.0. *Geoscientific Model Development*, 8, 2569–2586.

Tiedtke, M. (1989) A comprehensive mass flux scheme for cumulus parametrization in large-scale models. *Monthly Weather Review*, 117, 1779–1800.

Volonté, A., Clark, P.A. and Gray, S.L. (2018) The role of mesoscale instabilities in the sting-jet dynamics of windstorm *Tini*. *Quarterly Journal of the Royal Meteorological Society*, 144(712), 877–899.

Wernli, H. and Davies, H.C. (1997) A Lagrangian-based analysis of extratropical cyclones. I: The method and some applications. *Quarterly Journal of the Royal Meteorological Society*, 123, 467–489.

Wernli, H., Dirren, S., Liniger, M.A. and Zillig, M. (2002) Dynamical aspects of the life cycle of the winter storm '*Lothar*' (24–26 December 1999). *Quarterly Journal of the Royal Meteorological Society*, 128, 405–429.

Zängl, G., Reinert, D., Rípodas, P. and Baldauf, M. (2015) The ICON (ICOsahedral non-hydrostatic) modelling framework of DWD and MPI-M: description of the non-hydrostatic dynamical core. *Quarterly Journal of the Royal Meteorological Society*, 141, 563–579.

SUPPORTING INFORMATION

Additional supporting information may be found online in the Supporting Information section at the end of this article.

How to cite this article: Eisenstein L, Pantillon F, Knippertz P. Dynamics of sting-jet storm *Egon* over continental Europe: Impact of surface properties and model resolution. *Q J R Meteorol Soc*. 2020;146:186–210. https://doi.org/10.1002/qj.3666